Cell Metabolism

Article

Intracellular infection and immune system cues rewire adipocytes to acquire immune function

Graphical abstract

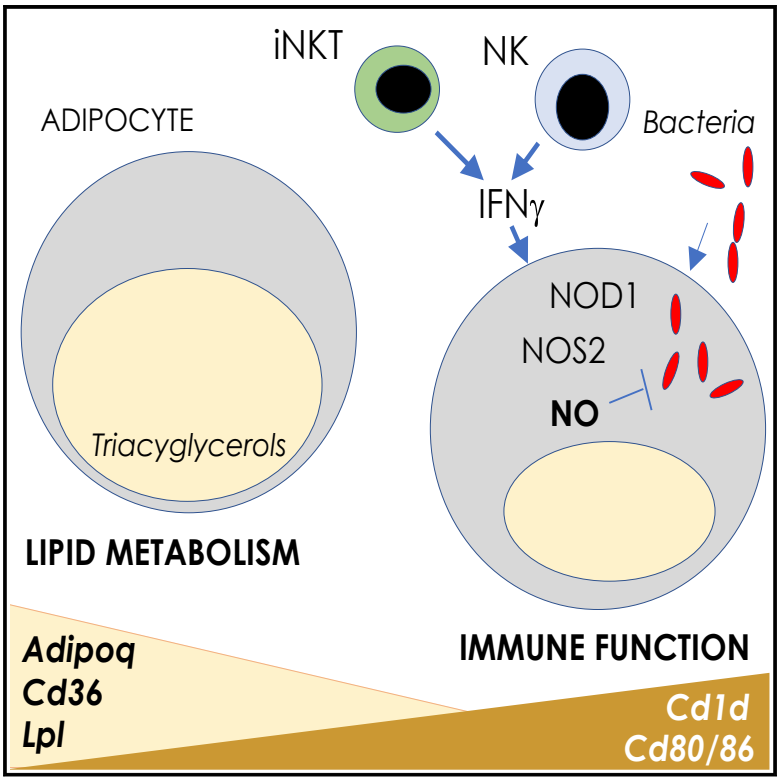

Highlights

- NK and iNKT cells make IFN-γ in response to bacterial infection in PAT
- IFN-γ induces NOD1-dependent iNOS expression in infected adipocytes
- Metabolic reprograming supports NO production in infected adipocytes
- Intrinsic NO production allows adipocytes to clear intracellular bacteria

Authors

George Caputa, Mai Matsushita, David E. Sanin, ..., Philipp Henneke, Erika L. Pearce, Edward J. Pearce

Correspondence

epearce6@jhmi.edu (E.L.P.), epearce7@jhmi.edu (E.J.P.)

In brief

Caputa and Matsushita et al. explored the role of perinodal adipose tissue (PAT) in the immune response to distal bacterial infection. They found that the infection spread to PAT, causing local IFN-γ- and NOD1-dependent *Nos2* expression by adipocytes, and the repurposing of these cells away from lipid metabolism toward fighting infection.

Caputa et al., 2022, Cell Metabolism *34*, 747–760
May 3, 2022
https://doi.org/10.1016/j.cmet.2022.04.008

CellPress

Cell Metabolism

CellPress

Article

Intracellular infection and immune system cues rewire adipocytes to acquire immune function

George Caputa,[1,12] Mai Matsushita,[1,12] David E. Sanin,[1,7] Agnieszka M. Kabat,[1] Joy Edwards-Hicks,[1] Katarzyna M. Grzes,[1] Roland Pohlmeyer,[2] Michal A. Stanczak,[1] Angela Castoldi,[1] Jovana Cupovic,[1] Aaron J. Forde,[3,4] Petya Apostolova,[1] Maximilian Seidl,[4,5,6] Nikki van Teijlingen Bakker,[1,3] Matteo Villa,[1] Francesc Baixauli,[1] Andrea Quintana,[1] Alexandra Hackl,[1] Lea Flachsmann,[1] Fabian Hässler,[1] Jonathan D. Curtis,[1] Annette E. Patterson,[1] Philipp Henneke,[7,8] Erika L. Pearce,[1,9,10,12,*] and Edward J. Pearce[1,3,9,11,12,13,*]

[1]Department of Immunometabolism, Max Planck Institute for Immunobiology and Epigenetics, 79108 Freiburg, Germany
[2]Imaging Facility, Max Planck Institute for Immunobiology and Epigenetics, 79108 Freiburg, Germany
[3]Faculty of Biology, University of Freiburg, 79104 Freiburg, Germany
[4]Center for Chronic Immune Deficiency, Faculty of Medicine, University of Freiburg, 79104 Freiburg, Germany
[5]Institute of Surgical Pathology, Faculty of Medicine, Medical Center, University of Freiburg, 79104 Freiburg, Germany
[6]Institute of Pathology, Heinrich Heine University and University Hospital of Duesseldorf, 40225 Duesseldorf, Germany
[7]Institute for Immunodeficiency, Center for Chronic Immunodeficiency, Medical Center and Faculty of Medicine, University of Freiburg, Freiburg, Germany
[8]Centre for Integrative Biological Signalling Studies, University of Freiburg, Freiburg, Germany
[9]Bloomberg Kimmel Institute, and Department of Oncology, Johns Hopkins University School of Medicine, Baltimore, MD 21287, USA
[10]Department of Biochemistry and Molecular Biology, Johns Hopkins University Bloomberg School of Public Health, Baltimore, MD 21287, USA
[11]Department of Molecular Microbiology and Immunology, Johns Hopkins University Bloomberg School of Public Health, Baltimore, MD 21287, USA
[12]These authors contributed equally
[13]Lead contact
*Correspondence: epearce6@jhmi.edu (E.L.P.), epearce7@jhmi.edu (E.J.P.)
https://doi.org/10.1016/j.cmet.2022.04.008

SUMMARY

Adipose tissue (AT) plays a central role in systemic metabolic homeostasis, but its function during bacterial infection remains unclear. Following subcutaneous bacterial infection, adipocytes surrounding draining lymph nodes initiated a transcriptional response indicative of stimulation with IFN-γ and a shift away from lipid metabolism toward an immunologic function. Natural killer (NK) and invariant NK T (iNKT) cells were identified as sources of infection-induced IFN-γ in perinodal AT (PAT). IFN-γ induced *Nos2* expression in adipocytes through a process dependent on nuclear-binding oligomerization domain 1 (NOD1) sensing of live intracellular bacteria. iNOS expression was coupled to metabolic rewiring, inducing increased diversion of extracellular L-arginine through the arginosuccinate shunt and urea cycle to produce nitric oxide (NO), directly mediating bacterial clearance. *In vivo*, control of infection in adipocytes was dependent on adipocyte-intrinsic sensing of IFN-γ and expression of iNOS. Thus, adipocytes are licensed by innate lymphocytes to acquire anti-bacterial functions during infection.

INTRODUCTION

Adipose tissue (AT) is a multifaceted organ responsible for the maintenance of systemic energy homeostasis. In addition to its classical role as a reservoir for excess energy through the storage of acquired and synthesized fatty acids (FAs) in the form of triglycerides (TAGs) (Chouchani and Kajimura, 2019), AT acts as an immunometabolic hub, both producing and responding to immunomodulatory adipokines and cytokines (Feingold et al., 1989, 1992; Hotamisligil et al., 1993; Patton et al., 1986) and hosting dynamic immune cell populations (Han et al., 2017; Kohlgruber et al., 2016).

While the role of AT in the setting of metabolic disease has been intensely investigated, the role of AT during an immune response to infection is still unclear. Recent work has shown that mesenteric AT juxtaposed to draining lymphatics from the intestine can become remodeled during *Yersinia pseudotuberculosis* infection following infiltration with immune cells, leading to permanent alterations in AT structure, immune cell composition, and microbiota permeability (Fonseca et al., 2015). Moreover, AT has the capacity to play an active role in host defense, as both differentiating and mature subcutaneous adipocytes were shown to secrete cathelicidin antimicrobial peptides during skin infection by *Staphylococcus aureus*

(Chavez-Arroyo and Portnoy, 2020; Pirzgalska et al., 2017; Wolf et al., 2017).

AT is intimately associated with lymphoid tissue, and many adipose depots host structures consisting of lymphoid cell clusters (Moro et al., 2010; Pond, 1996). This AT immediately proximal to lymph nodes (LNs), termed perinodal AT (PAT), has been reported to have unique characteristics compared to white and brown adipose deposits, including increased expression of tumor necrosis factor (TNF) receptor in response to lipid polysaccharide (LPS) (MacQueen and Pond, 1998), enriched polyunsaturated lipid content (Acedo et al., 2011; Mattacks and Pond, 1997), hypervascularization in response to local immune stimuli (Macqueen et al., 1999), and a fluidic continuity with lymphatics (Lin et al., 2018). Due to the rapid proliferation of lymphocytes during the mounting of an adaptive immune response (Williams and Bevan, 2007), the requirement for exogenous lipid by $CD8^+$ T lymphocytes (O'Sullivan et al., 2014), and the ability of AT to support proliferating cell populations (Nieman et al., 2011), we hypothesized that PAT surrounding LNs may provide factors necessary to support $CD8^+$ T cell proliferation during a developing immune response.

Here we explore the role of PAT in the immune response to *Listeria monocytogenes* (*Lm*), an intracellular pathogen that has an important role in foodborne disease and neonatal sepsis. Resolution of *Lm* infection is dependent on endogenous IFN-γ production (Buchmeier and Schreiber, 1985). We find that loss of mature adipocytes within PAT, or of the ability of PAT to mobilize stored TAGs, has no effect on the clearance of an acute *Lm* infection from the site of infection, or on the developing $CD8^+$ T cell response within LNs draining the site of infection. However, over the course of infection PAT itself becomes infected, and signals from intracellular bacteria via nuclear-binding oligomerization domain 1 (NOD1) and from infiltrating NK and iNKT cells via IFN-γ result in the remodeling of adipocyte function away from energy storage toward an immunological role. In this immunologically activated state, adipocytes express inducible nitric oxide synthase (iNOS) and are metabolically reprogramed to support the generation of NO to locally control infection within the PAT. This work highlights a previously uncharacterized antimicrobial function of PAT and extra-metabolic capacity of adipocytes to actively participate in the immune response to bacterial infection.

RESULTS

PAT is not required to mount a T cell response to clear *Lm*

We speculated that, due to its proximal location to LNs, PAT could be supporting the development of the adaptive immune response during infection. To explore this, we subcutaneously injected 1×10^6 CFU of *Lm* into the rear footpad of mice and analyzed PAT surrounding the draining popliteal LN (PLN). Twenty-four hours after infection, the PAT and PLN exhibited increased size and weight compared to the contralateral PAT and PLN, which were proximal to a PBS-injected footpad (PBS PAT), and PAT from a control mouse (ctrl PAT), which received PBS injections in both hind footpads (Figures 1A and 1B). Weight increases in PAT persisted for 3 days after infection (Figure 1B). Using MRI, we determined that the increase in weight coincided not with an increase in fat mass (Figure 1C) or TAGs (Figure 1D), but rather with a rapid increase in lean mass (Figure 1E). Imaging of the PAT coupled with flow cytometric analysis of the stromal vascular fraction (SVF) suggested that the increase in lean mass reflects infiltration by cells of hematopoietic origin (Figures 1F and 1G).

We hypothesized that PAT could support the rapid proliferation of lymphocytes in the proximal LN. However, while MRI analysis indicated a slight drop in fat content on day 2 post-infection, which would coincide with rapid T cell expansion, TAGs in adipocytes isolated from PAT were unchanged as a result of infection 24 h following infection (Figures 1C and 1D). To specifically address the contribution of adipocytes to an acute immune challenge, we measured infection-induced changes in $Pparg^{fl/fl}$ *Adipoq*-Cre^{ERT2} mice, which lack mature adipocytes (Figures S1A and S1B), and $Pnpla2^{fl/fl}$ *Adipoq*-Cre mice, which lack adipocyte triacylglycerol lipase (ATGL, *Pnpla2*) (Figure S1C), and therefore the ability to liberate free FAs. Phenotyping of features within the PLN associated with the development of immunity to *Lm* revealed no difference in the numbers of cells (Figures S1D and S1L), bacterial CFUs (Figures S1E and S1M), infection-specific $CD8^+$ T cells (Figures S1F, S1G, S1N, and S1O), $CD44^{hi}$ (activated) $CD8^+$ T cells (Figures S1H and S1P), proliferating $CD8^+$ T cells (Figures S1I and S1Q), or IFN-γ (Figures S1J and S1R) and TNF (Figures S1K and S1S)-producing $CD8^+$ T cells, as a result of the loss of PAT, or ATGL within PAT. These data indicate that, contrary to our expectations, PAT is not required for the development of a $CD8^+$ T cell response in this model of acute bacterial infection, nor for protective immunity.

Infected adipocytes within PAT are rapidly cleared of bacteria

Despite the lack of acute effects upon loss of PAT or ATGL on adaptive immunity, we were intrigued by the infiltration of immune cells in PAT, which raised the possibility of local bacterial infection distal to the site of bacterial inoculation. Without appropriate cell-mediated immunity, *Lm* can become systemic, and indeed this characteristic is a reason for the high mortality rates associated with this infection in immunocompromised individuals (Vazquez-Boland et al., 2001). Following footpad infection, we were able to isolate viable bacteria from the PAT as well as the foot and the PLNs of legs injected with *Lm*. Over the 3 days following infection, we noted a 10^3-fold decrease in CFUs in PAT, with a 10-fold decrease in CFUs in the neighboring PLNs, and no control of infection in the foot during this time (Figure 1H). Since *Lm* has broad host cell specificity (Vazquez-Boland et al., 2001), we asked whether the adipocytes themselves, or SVF cells within the PAT, were infected. We found similar numbers of bacteria were present in the adipocyte and SVF fractions 24 h following infection, but that bacteria in the adipocyte fraction were cleared more quickly over the following 2 days than in either the SVF or the PLNs (Figure 1I). These results were corroborated by a model of ear infection with the skin pathogen *S. aureus*, where infection within the PAT surrounding the draining parotid LN was apparent within 24 h, and adipocytes and SVF were equivalently infected. As in the PAT around PLNs of mice infected with *Lm*, the adipocytes were able to control the *S. aureus* infection more rapidly than were cells in the SVF (Figure 1J).

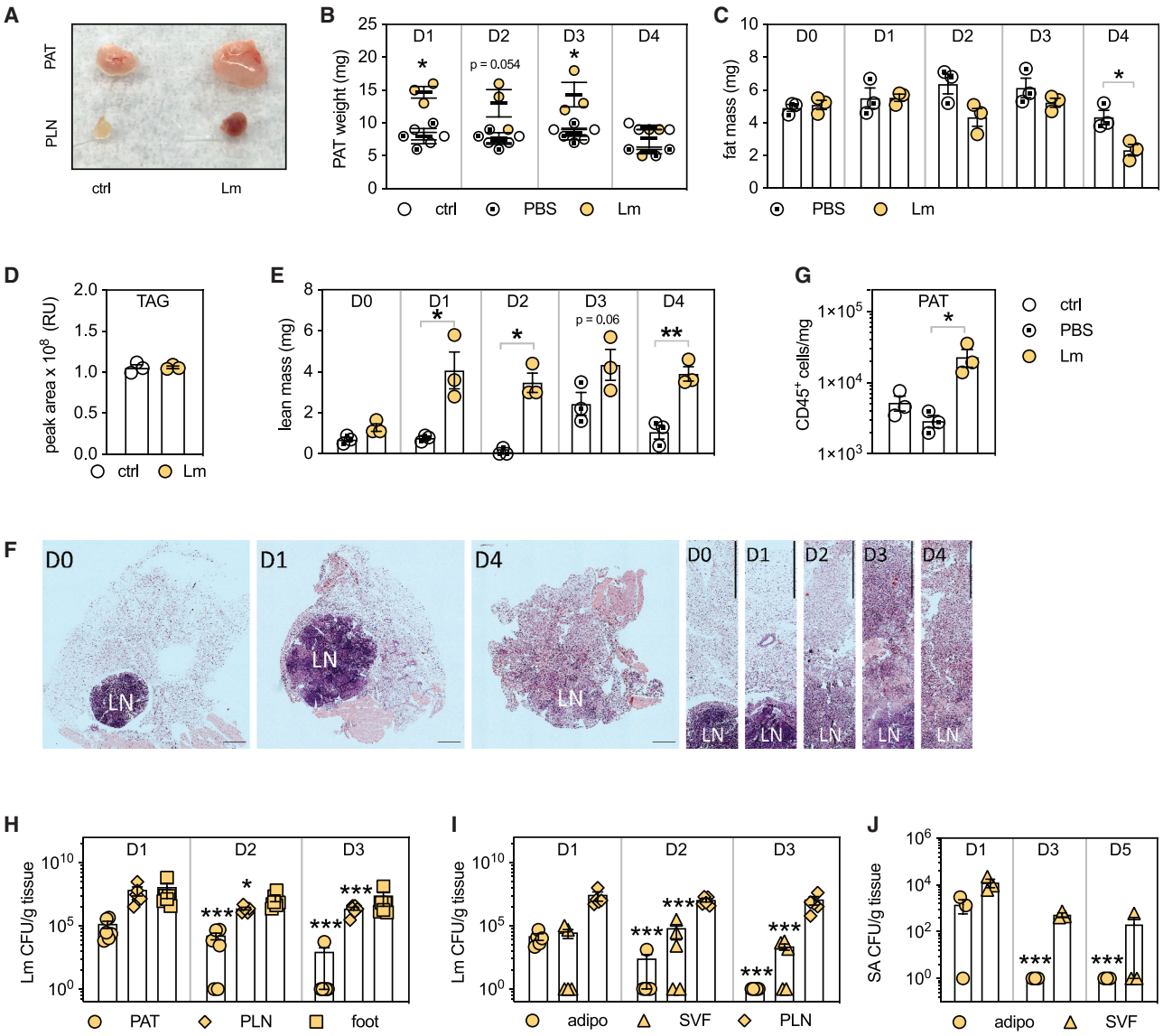

Figure 1. PAT becomes infected upon exposure to *L. monocytogenes*, which is rapidly cleared from adipocytes

(A and B) WT mice received a footpad injection of 1 × 10^6 CFU *L. monocytogenes* (*Lm*) and PBS contralaterally or were sham infected with PBS in both hind footpads (ctrl). Twenty-four hours following infection, perinodal AT (PAT) around popliteal lymph nodes (PLN) was harvested (A) and PAT was weighed (B) and analyzed further.

(C and E) Fat (C) and lean (E) mass were measured using Echo-MRI.

(D) *Lm*-infected PAT was fractionated into adipocytes (adipo) and stromal vascular fraction (SVF) 24 h post-infection. Triglycerides (TAGs) were extracted from adipocytes and measured using LC-MS.

(F) H&E staining of PAT and PLN 1–4 days post-infection. Lymph node, LN; scale bars, 500 μm.

(G) Flow cytometric quantification of $CD45^+$ cells per gram of tissue indicated.

(H) *Lm*-infected PAT, PLN, or foot was homogenized and CFUs per gram of tissue were calculated.

(I) *Lm*-infected PAT was fractionated into adipocytes and stromal vascular fraction . CFUs per gram of tissue were calculated.

(J) WT mice received an ear injection of *S. aureus* or were sham infected with PBS. 1, 3, and 5 days following infection, perinodal adipose surrounding the parotid lymph node was fractionated into adipocytes and stromal vascular fraction. CFU per gram of tissue was calculated.

Statistical significance was calculated using two-tailed Student's t test (*$p < 0.05$, **$p < 0.005$, ***$p < 0.0005$, *Lm* versus control or PBS) or negative binomial regression (compared to D1; H–J). Mean ± SEM from 3 (B–E, G, and J), 5 (I), or 6 (H) biological replicates. Representative data from at least three independent experiments.

Infection redirects adipocytes toward host defense

To explore the response of adipocytes to bacterial infection, we examined changes in gene expression of *ex vivo* isolated perinodal adipocytes following *Lm* infection using RNA sequencing (RNA-seq) (Figure 2A). Compared to adipocytes from PBS PAT (PBS injection control with contralateral *Lm* infection) and ctrl PAT (uninfected and injected with PBS), adipocytes from *Lm* PAT displayed extensive changes in gene expression

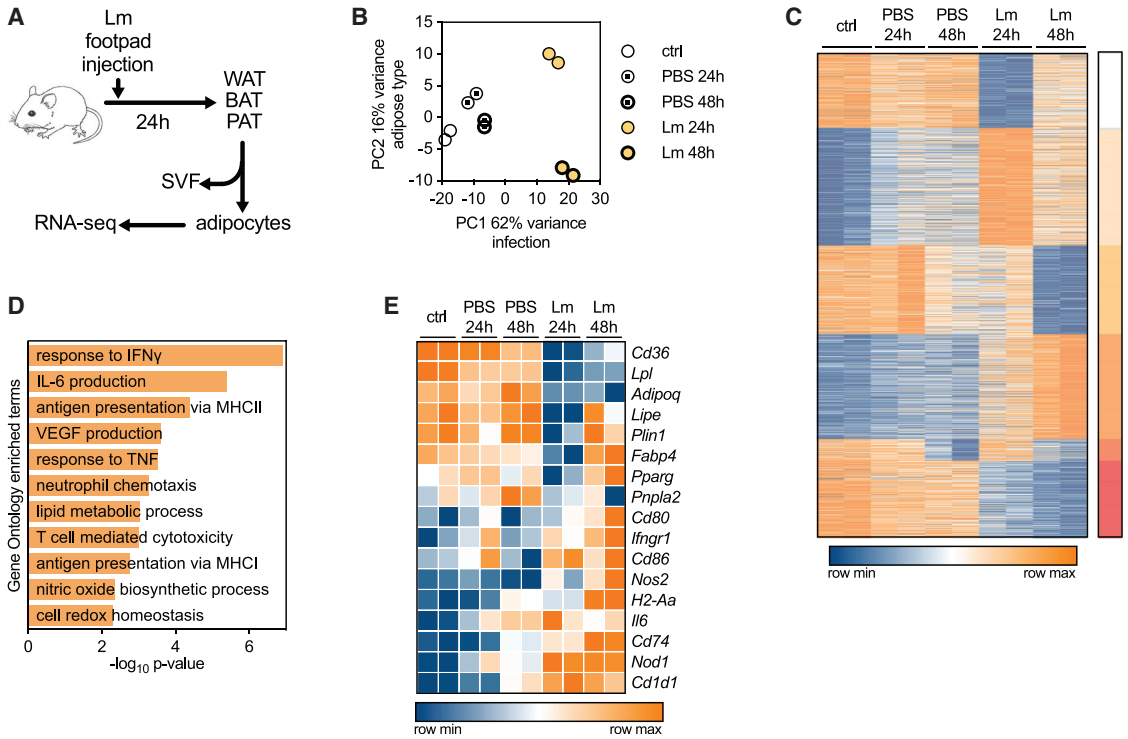

Figure 2. Infection redirects adipocytes toward host defense

(A) Schematic of sample preparation for adipocyte RNA-seq.

(B) PCA of adipocyte RNA-seq from control, PBS, and *Lm* PAT at 24 and 48 h post-infection.

(C) K-means clustering of genes with both statistically significant and greater than 2-fold expression compared to control adipocytes.

(D) Gene ontology pathway analysis of genes that were significantly enriched in *Lm* samples at 24 and 48 h, but not PBS or control.

(E) Heatmap depicting canonical adipocyte- and immune-associated genes.

Data show two biological replicates per group.

(Figures 2B and 2C). GO analysis of genes differentially expressed during infection highlighted a suite of metabolism-, immune-, and inflammation-related gene networks (Figure 2D). The expression of several genes involved in lipid metabolism *(Cd36*, *Lpl*, and *Adipoq*), the canonical function of adipocytes, was downregulated over time after infection, whereas the expression of a host of genes associated with immune function (*Cd86*, *Nos2*, *Ifngr1*, *Cd80*, *Il6*, *Cd74*, *H2-Aa*, *Cd1d1*, and *Nod1*) was induced (Figure 2E). The expression of several cytokine receptor genes, including *Ifnar1,2* and *Ifngr1,2*, was upregulated in adipocytes in PAT surrounding *Lm* PAT and in PBS PAT from the same mice (Figure S2A). Intriguingly, expression of the receptor for the adipokine IL-6 decreased as a result of infection (Figure S2A). Macrophages can be intimately associated with adipocytes; however, the changes we observed in gene expression within the adipocyte fraction did not reflect contamination with macrophages, as we observed no enrichment in transcripts corresponding to classical macrophage markers (Figure S2B). These data suggest a marked functional refocusing of adipocytes during infection away from fat metabolism and toward host defense.

IFN-γ production by NK and iNKT cells drives changes in PAT adipocytes

To more fully explore the nature of infection-induced changes in the SVF, and to identify the source of IFN-γ responsible for activating adipocytes to express *Nos2*, we performed single-cell RNA-seq (scRNA-seq) on SVF from *Lm*-, PBS-, and ctrl-PAT at 24 h post-infection (Figure 3A). Individually sequenced cells were arranged in 26 transcriptionally distinct clusters that could be mapped to specific cell types (Figures S3A, S3B, and S3D). We observed that *Lm* infection resulted in the appearance in the SVF of a large number of cells expressing *Ptprc*, which encodes CD45 (Figures 3B and 3C), matching our earlier results. We identified macrophages, monocytes, dendritic cells, neutrophils, B cells, $CD8^+$ T cells, NK cells, and NKT cells within the $CD45^+$ population; however, ILC1 cells were not detected (Figure 3D). Macrophage/monocytes and neutrophils were a prominent feature of the response to infection (Figure S3A). We next examined *Ifng* mRNA and observed it being predominantly expressed in NK cells and NKT cells (Figures 3D and 3E), which prompted us to examine these cells in more detail. Upon re-clustering (Figure 3F), we confirmed the presence of two IFN-γ-producing cell types, NK and iNKT cells (Figure 3G), based on their overall transcriptional profiles (Figure S4A) and specifically the expression of *Klrb1c* by NK cells, and additionally *Cd3d* by iNKT cells (Figure 3H). Flow cytometric analysis of infected PAT confirmed the presence of IFN-γ-expressing NK and iNKT cells (Figures S4B–S4E) in *Lm* PAT. *In vivo* targeting using antibodies that deplete NK and iNKT cells (α-NK1.1 and α-Asialo-GM1) and block antigen presentation to iNKT cells (α-CD1d) resulted in a reduction in NK

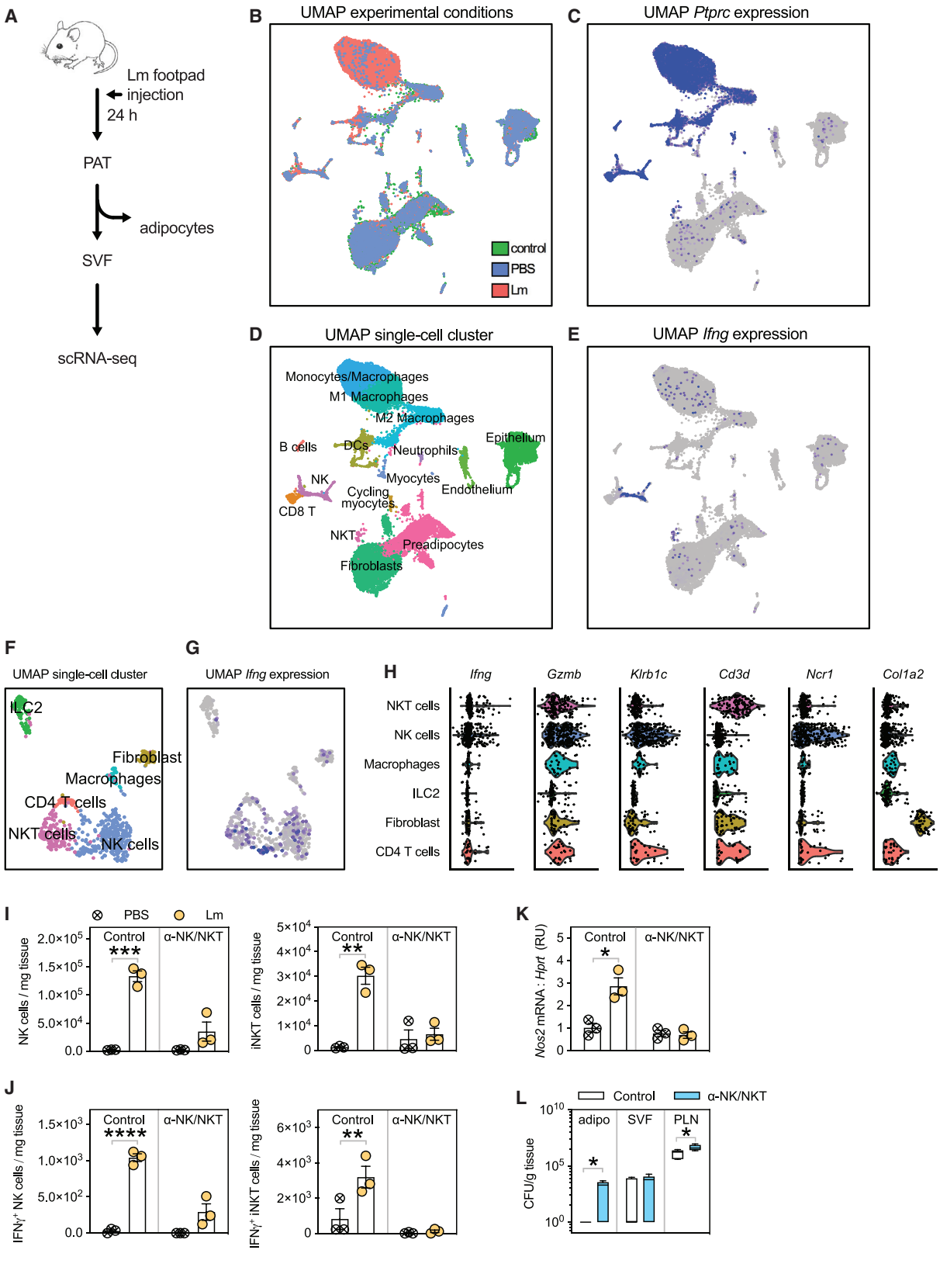

(legend on next page)

and iNKT cells (Figure 3I), and specifically in IFN-γ-producing NK and iNKT cells (Figure 3J), in PAT at 48 h following infection. This correlated with a failure of adipocytes to express *Nos2* mRNA (Figure 3K) and clear *Lm* (Figure 3L). Taken together, these data establish an activation axis, whereby IFN-γ-producing NK and iNKT cells are recruited to PAT following infection, thereby activating cell-intrinsic antimicrobial gene expression in infected adipocytes that is important for host defense.

IFN-γ induces iNOS expression in infected adipocytes

To formally exclude the possibility that immune gene expression by adipocytes in *Lm* PAT was a reflection of contaminating immune cells, we asked whether observed changes in gene expression were recapitulated in 3T3-L1 preadipocyte-derived adipocytes cultured with *Lm in vitro.* We observed that exposure to *Lm* alone had modest effects compared to the changes we had observed in PAT adipocytes following infection *in vivo* (Figure 4A). However, when we exposed the adipocytes to *Lm* in combination with IFN-γ, a cytokine strongly induced by *Lm* infection (Pamer, 2004), we observed decreased expression of lipid metabolism genes and increased expression of immune genes (Figure 4A), a signature that closely matched the results from the *Lm* PAT adipocytes (Figure 2E). The expression of known IFN-γ-induced genes, such as *Cd74*, was increased in response to IFN-γ alone (Figure 4A) (Schroder et al., 2004).

Among the genes expressed by adipocytes *in vivo* following *Lm* infection and *in vitro* in response to *Lm* plus IFN-γ was *Nos2.* This gene encodes iNOS, an enzyme that generates NO from arginine. NO can diffuse across membranes, is bactericidal, and has been heavily implicated in the immune response to *Lm* (MacMicking et al., 1995). Expression of iNOS in macrophages requires additional signals, including IFN-γ or TNF, in concert with pathogen-derived signals (Weisz et al., 1994), and our data implied that this was also the case for adipocytes. Infection of 3T3-L1-derived adipocytes with *Lm* in the presence of both IFN-γ and TNF synergized to induce *Nos2* mRNA (Figure 4B), and *Lm* plus IFN-γ induced iNOS protein expression (Figure 4C). Neither cytokine alone nor *Lm* alone had these effects (Figures 4B and 4C). Mature adipocytes differentiated from *ex vivo* isolated inguinal preadipocytes exhibited similar increases in *Nos2* mRNA and iNOS protein (Figures 4D and 4E). Similarly, we were able to detect *Nos2* mRNA in *ex vivo* isolated mature adipocytes from *S. aureus*-infected AT (Figure 4F). *Ifngr1* knockout *ex vivo* differentiated adipocytes exhibited defective iNOS induction in the presence of Lm and IFN-γ, while TNF was insufficient to induce substantive iNOS expression, further indicating that IFN-γ stimulation is specifically required in adipocytes for iNOS expression (Figure 4G; we speculate that the IFN-γ-induced iNOS band in the *Ifngr1*-deficient cells represents the response of preadipocytes that have yet to fully differentiate into mature adipocytes and express *Adipoq*, and which therefore continued to be responsive to IFN-γ).

NOD1 is required for induction of iNOS by adipocytes during infection

Bacterial products can be sensed by cell surface or intracellular pattern recognition receptors (PRRs), which in macrophages are sufficient to trigger iNOS expression in the presence of IFN-γ (Silva et al., 2010). Only treatment of mature 3T3-L1 adipocytes with IFN-γ and live *Lm*, as compared to heat inactivated (HI) *Lm* or with LPS, was sufficient to induce iNOS expression (Figures 5A and 5B). These results suggested that an intracellular PRR is important for the adipocyte response, and therefore that it is actively infected cells that are expressing iNOS.

We noted that expression of *Nod1* was elevated in adipocytes isolated from *Lm* PAT (Figure 2E), in 3T3-L1cells stimulated with IFN-γ alone, and more markedly, after exposure to IFN-γ plus *Lm* (Figure 4A). We reasoned that this cytoplasmic PRR could serve as the sensor for *Lm* infection in adipocytes exposed to IFN-γ (Opitz et al., 2006). We found that iE-DAP, a NOD1-specific agonist, together with IFN-γ, was sufficient to induce iNOS expression in adipocytes, while ML130, a NOD1-specific antagonist, blocked expression of iNOS in adipocytes exposed to *Lm* plus IFN-γ (Figure 5C). CRISPR knockout of NOD1 in 3T3-L1 differentiated adipocytes abrogated the induction of iNOS by *Lm* infection and IFN-γ treatment (Figure 5D). IFN-γ signals through the activation of the JAK-STAT pathway, whereby phosphorylated STAT1 binds to the promoter of interferon-stimulated genes and promotes their transcription (Schroder et al., 2004). We observed that IFN-γ treatment alone was sufficient to induce STAT1 phosphorylation in adipocytes (Figure S5). Taken together, these data demonstrate that IFN-γ induces the expression of NOD1, and that this PRR serves as an intracellular sensor for bacterial infection to synergize with IFN-γ-induced signaling to promote iNOS expression in adipocytes.

Infection rewires metabolism in PAT adipocytes to support NO production

Adipocytes stimulated to express iNOS with *Lm* plus IFN-γ produce NO, measured in tissue culture medium as nitrite

Figure 3. NK/iNKT cell-derived IFN-γ induces iNOS expression in adipocytes following infection

(A) Schematic of sample preparation for scRNA-seq.

(B–E) Clustered UMAP plot of SVF colored by (B) treatments or (C) *Ptprc* expression (blue), (D) single-cell cluster cell-type annotations, or (E) *Ifng* expression (blue).

(F and G) Clustered UMAP plot of *Ifng*$^+$ cells.

(H) Violin plot of cell-type-defining genes.

(I–L) WT mice were injected with control purified mouse IgG2a or with a cocktail of 40 μg α-NK1.1, 40 μg α-CD1d, and 35 μL α-Asialo-GM1 antibodies 24 h before infection and analyzed 2 days post-infection (d.p.i.).

(I and J) Flow cytometric quantification of (I) CD3$^-$CD338$^+$NK1.1$^+$ NK (left) or Cd1d-tetramer$^+$CD3$^+$NK1.1$^+$ iNKT cells (right), and (J) IFNγ$^+$ cells of NK (left) or iNKT (right) per milligram of tissue from infected PAT (*Lm*).

(K) qRT-PCR analysis of *Nos2* mRNA normalized to *Hprt* expression from *Lm*-infected adipocytes.

(L) CFUs per gram of tissue were calculated from *Lm*-infected adipocytes, SVF, and PLNs.

Statistical significance was calculated using two-tailed Student's t test (*$p < 0.05$, **$p < 0.005$, α-NK/iNKT versus control). Mean ± SEM from three to four biological replicates. Representative data of 3 (I–K) or 4 (L) biological replicates per group from 3 (I–L) independent experiments.

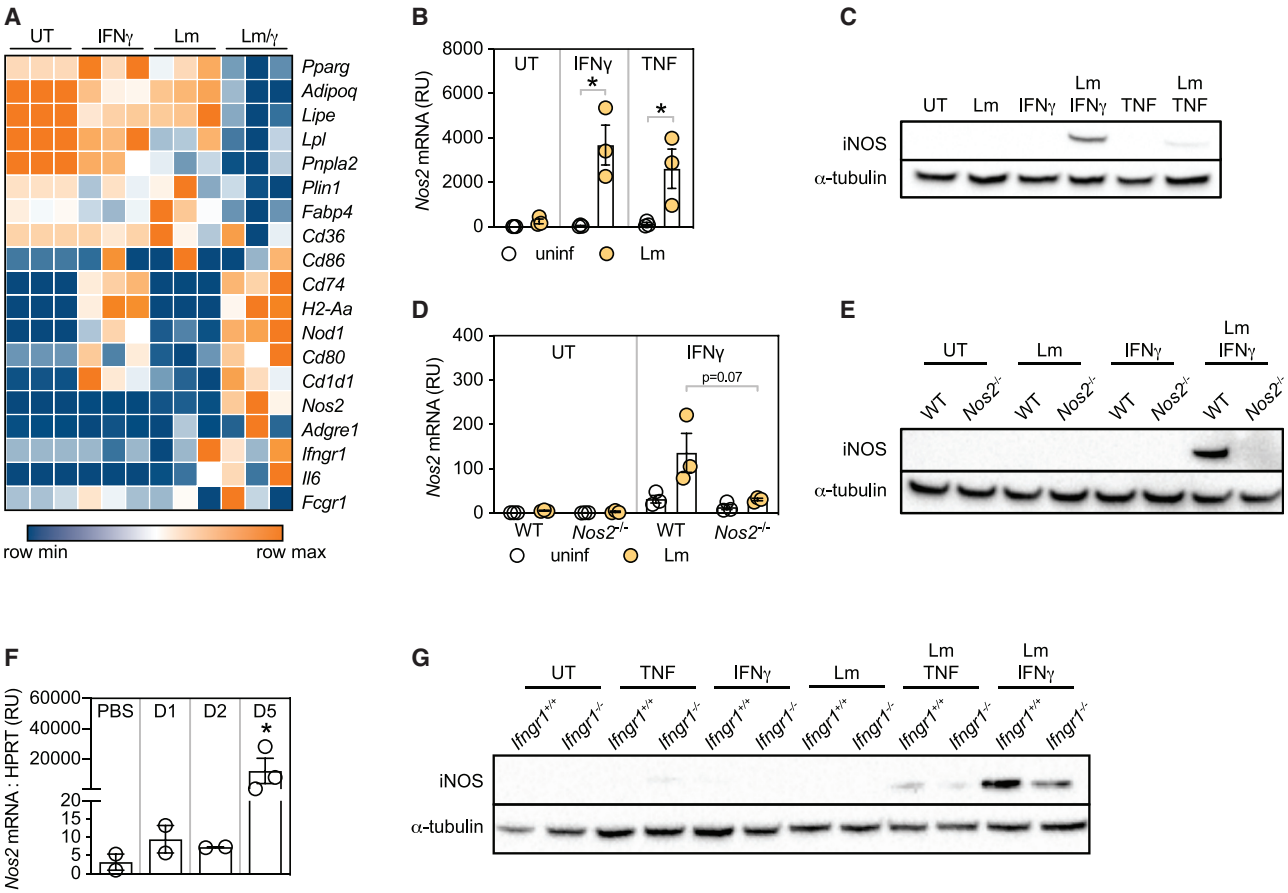

Figure 4. IFN-γ induces iNOS expression in infected adipocytes

(A–C) 3T3-L1 or (D and E) mouse inguinal preadipocytes were differentiated into mature adipocytes for 7 days, followed by infection with *L. monocytogenes* (*Lm*) at an MOI of 50 in the presence of indicated cytokines for 24 h.

(A) Heatmap depicting qRT-PCR measurements of indicated genes.

(B and D) qRT-PCR analysis of *Nos2* mRNA normalized to *Hprt* expression.

(C and E) Representative western blot of iNOS and α-tubulin protein.

(F) WT mice received an ear injection of *S. aureus* or were uninfected. 1, 2, and 5 days following infection, perinodal adipose surrounding the parotid lymph node was fractionated and analyzed by qRT-PCR. NOS2 mRNA normalized to *Hprt* expression shown.

(G) Inguinal preadipocytes from *Ifngr1*$^{+/+}$ (*Ifngr1*$^{fl/fl}$) or *Ifngr1*$^{-/-}$ (*Ifngr1*$^{fl/fl}$ *Adipoq-Cre*) mice were differentiated into mature adipocytes for 7 days, followed by infection with *L. monocytogenes* (*Lm*) at an MOI of 50 in the presence of IFN-γ. Immunoblot of iNOS and α-tubulin protein. Representative of two independent experiments.

Statistical significance was calculated using two-tailed Student's t test (*$p < 0.05$, **$p < 0.005$, treatment versus uninfected or control group versus knockout group). Mean ± SEM from 3 (B and D) or 2–3 (F) biological replicates. Representative data from three (B–F) and two (G) independent experiments.

(Figure 6A), through a *Nos2*-dependent pathway (Figure 6B), and iNOS expression was required for bacterial clearance *in vitro* (Figure 6C). NO is a potent inhibitor of electron transport chain (ETC) complex I (Clementi et al., 1998), and we reasoned that, as adipocytes primarily utilize glucose-fueled mitochondrial oxidative phosphorylation (OXPHOS) for ATP generation and *de novo* lipogenesis (Chouchani and Kajimura, 2019), infected adipocytes might exhibit metabolic changes as a result of NO generation (Everts et al., 2012; Jha et al., 2015). Extracellular flux analysis of 3T3-L1-derived mature adipocytes revealed that infection alone does not alter the oxygen consumption rate (OCR) or extracellular acidification rate (ECAR), proxy measures of OXPHOS and glycolysis, respectively (Figure 6D). However, we measured a drop in OCR following IFN-γ treatment of infected adipocytes, presented as a decline in OXPHOS, along with a simultaneous increase in ECAR, indicating an increased commitment to aerobic glycolysis to fulfill metabolic requirements (Figures 6D and 6E). Acute treatment of infected adipocytes in the presence of IFN-γ with the iNOS-specific inhibitor 1400W was sufficient to reverse this metabolic shift (Figures 6D and 6E). Measurements of metabolic changes in adipocytes derived from *Nos2*$^{-/-}$ preadipocytes concurred with data from wild-type (WT) cells treated with iNOS inhibitors (Figure 6F). Consistent with the Nod1 dependence of iNOS expression, IFN-γ-induced bacterial clearance and elevated ECAR were inhibited by Nod1 antagonism (Figure 6G and 6H), indicating an essential role for NOD1 in adipocyte metabolic rewiring linked to the acquisition of immune functions.

In order to better understand the dynamic metabolic changes occurring within infected adipocytes, we performed metabolomic

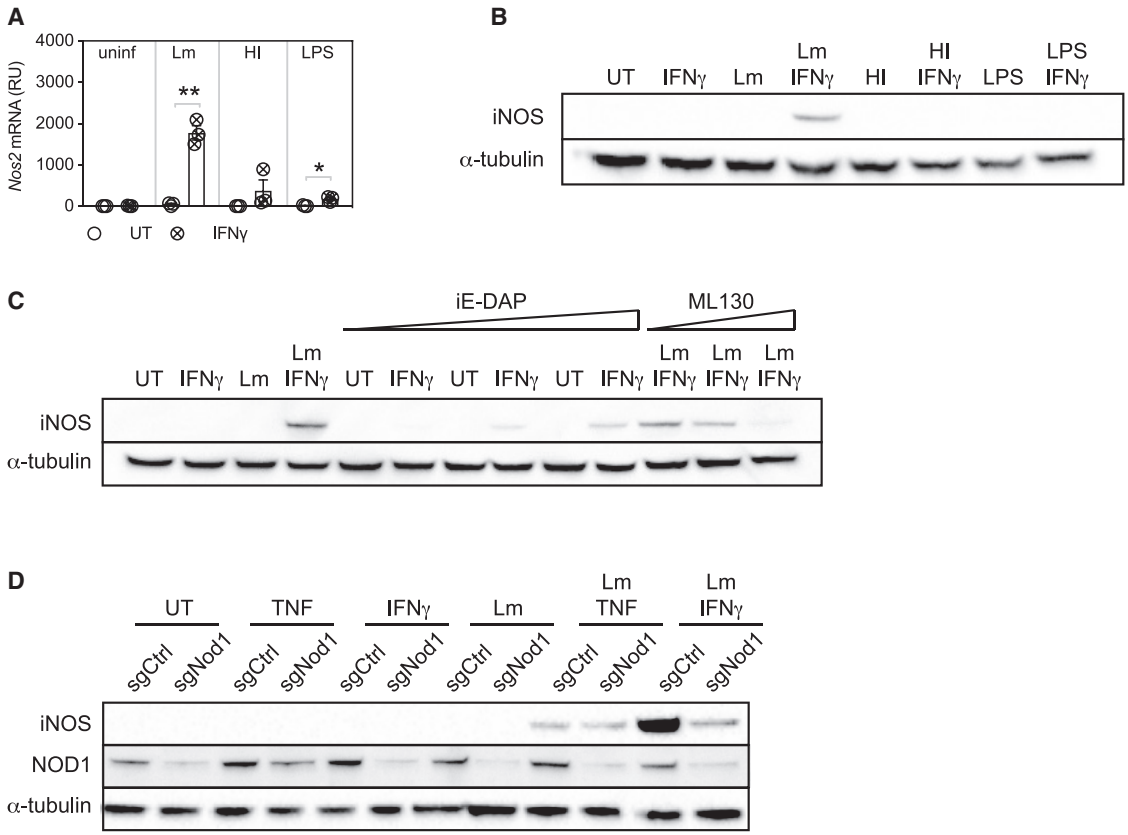

Figure 5. iNOS induction is NOD1 dependent

(A and B) 3T3-L1-derived mature adipocytes were infected with live *Lm* or treated with heat-inactivated (HI) *Lm* for 1 h, or with lipopolysaccharide (LPS) for 24 h in the presence of IFNγ.

(A) qPCR analysis of *Nos2* mRNA normalized to *Hprt* expression.

(B) Western blot of iNOS and α-tubulin protein.

(C) 3T3-L1-derived mature adipocytes were either treated for 24 h in the presence of the NOD1 agonist iE-DAP with or without IFNγ, or infected with live *Lm* and treated for 24 h with IFN-γ and the NOD1 inhibitor ML130. Western blot of iNOS and α-tubulin protein.

(D) 3T3-L1 CRISPR knockout clones were infected with *Lm* in the presence of TNF or IFNγ. Representative western blot of iNOS, NOD1, and α-tubulin protein. Statistical significance was calculated using two-tailed Student's t test (*$p < 0.05$, **$p < 0.005$, treatment versus untreated). Mean ± SEM from at least three biological replicates. Representative data from three independent experiments.

analyses using mass spectrometry (MS). Hierarchical clustering of metabolites quantified by gas chromatography-MS (GC-MS) and liquid chromatography-MS (LC-MS) revealed that metabolites in the argininosuccinate shunt and urea cycle were increased in infected adipocytes exposed to IFN-γ, as compared to infected adipocytes alone (Figures S6A and S6B). As noted previously, parallel increases in metabolite pools common to the arginosuccinate shunt, urea cycle, and TCA cycle, as observed here (Figures S6A and S6B), are characteristic of metabolites partaking in common metabolic cycles (Jha et al., 2015). ^{13}C-metabolite tracing of glucose, glutamine, palmitate, and arginine further revealed that extracellular arginine comprised the majority of the intracellular arginine pool within the urea cycle (Figure 6I). This metabolic rewiring is a hallmark of NO-producing cells, as the argininosuccinate shunt supports increased arginine demand in iNOS-expressing cells by converting ornithine, a byproduct of NO production, back into arginine (Rath et al., 2014). The increased arginine flux into infected adipocytes was required to fuel NO production, but not for general metabolic homeostasis, as infected adipocytes incubated in arginine-free media were unable to produce nitrite, but able to respire normally (Figures 6J and 6K). This is consistent with the lack of ^{13}C-arginine label in TCA cycle intermediates (Figure 6I). These data demonstrate that infected adipocytes in the presence of IFN-γ require extracellular arginine to fuel NO production, and that this is associated with metabolic reprogramming toward aerobic glycolysis.

Interestingly, while lipidomics of adipocytes from *Lm*-infected PAT revealed no differences in major classes of lipids, the only enriched lipid species detected was hexosylceramide (Figures S6C and S6D), the activating ligand for iNKT cells (Brennan et al., 2013).

IFN-γ signaling and iNOS expression are required for bacterial clearance in infected adipocytes

We reasoned that if IFN-γ is critical for adipocyte-intrinsic defense against *Lm*, then adipocyte-specific deletion of *Ifngr1* should impair antimicrobial activity of PAT. We examined this in *Ifngr1*$^{fl/fl}$ *Adipoq-Cre* mice, in which *Ifngr-1* is deleted

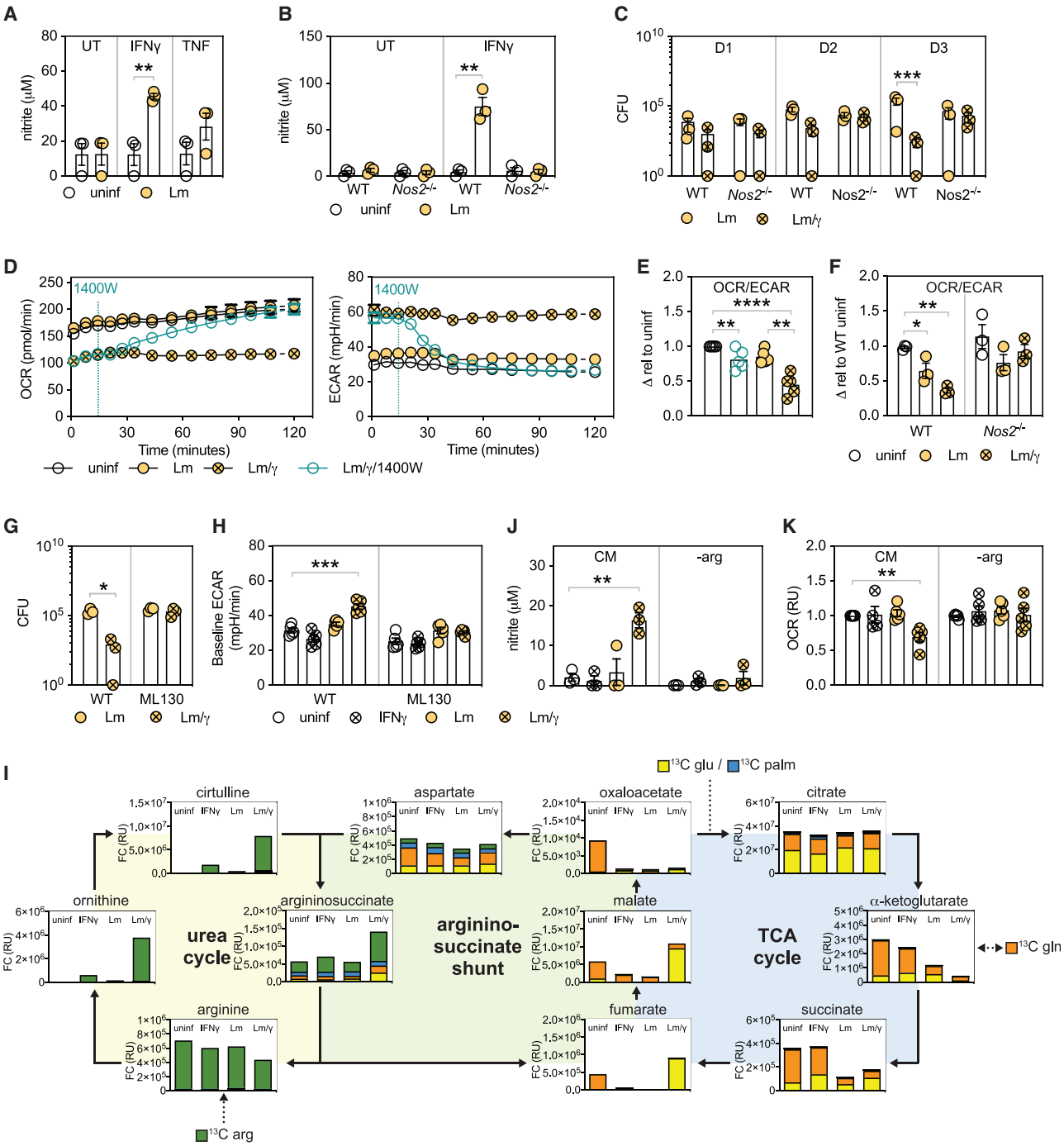

Figure 6. Infected adipocytes engage the argininosuccinate shunt to support NO production

3T3-L1 (A, D, E, and G–K) or inguinal preadipocytes from WT or iNOS$^{-/-}$ mice (B, C, and F) were differentiated into mature adipocytes for 7 days. Mature 3T3-L1-derived adipocytes were treated with 50 μM ML130 for 24 h prior to *Lm* infection (G and H). On day 7, adipocytes were infected with *Lm* at an MOI of 50 in the presence of IFNγ.

(A and B) Nitrite levels in the supernatant were analyzed by Griess reaction.

(C) CFUs were calculated at indicated d.p.i.

(D and E) Dotted line denotes injection of 1400W, a specific inhibitor of iNOS.

(D) Representative plot of oxygen consumption rate (OCR; right) and extracellular acidification rate (ECAR; left) measured by Seahorse Extracellular Flux Analyzer.

(E) Summary of OCR/ECAR ratio normalized to uninfected.

(F) Summary of OCR/ECAR ratio normalized to uninfected.

(G) CFUs were calculated at 3 d.p.i.

(H) Baseline ECAR was measured by Seahorse Extracellular Flux Analyzer 1 d.p.i.

(legend continued on next page)

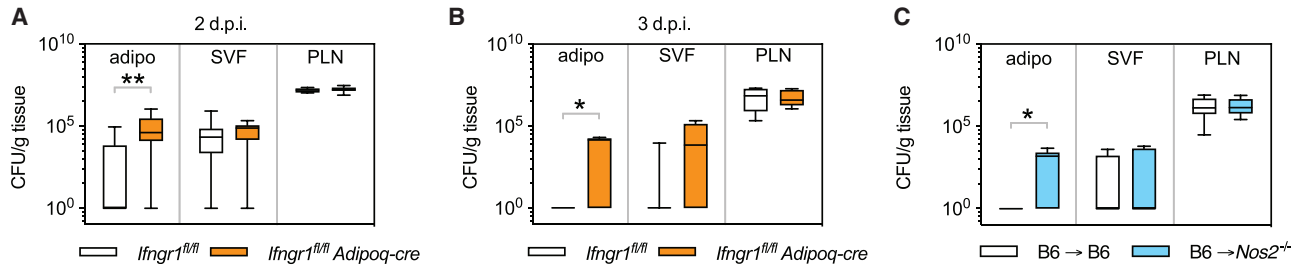

Figure 7. Adipocytes require IFN-γ signaling to induce iNOS expression for *Lm* clearance

(A and B) *Ifngr1*$^{fl/fl}$ or *Ifngr1*$^{fl/fl}$ *Adipoq*-Cre mice received a footpad injection of 1 × 10^6 CFU *Lm*. PAT was fractionated into adipocytes (adipo) and stromal vascular fraction (SVF) at 2 d.p.i. (A) and 3 d.p.i. (B). CFUs per gram of tissue were calculated for adipo, SVF, and PLNs.

(C) Lethally irradiated WT and *Nos2*$^{-/-}$ mice were reconstituted with congenically marked Ly5.1$^+$ WT bone marrow cells and infected with *Lm* 8–9 weeks post-reconstitution. CFUs were calculated at 3 d.p.i.

Statistical significance was calculated using two-tailed Student's t test (*$p < 0.05$, **$p < 0.005$, control group versus knockout group). Mean ± SEM from 8–9 (A), 4 (B), and 10 (C) biological replicates. Representative data from two (B), three (C), and four (A) independent experiments.

specifically in adipocytes, and found that sterilization of PAT during infection was significantly impaired (Figures 7A and 7B; later time points were not examined). This deletion had no effect on the *Lm* burden in the SVF or PLNs. Furthermore, to investigate the contribution of adipocyte-intrinsic iNOS, we generated WT to *Nos2*$^{-/-}$ bone marrow chimeras, which revealed reduced capacity to clear *Lm* in adipocytes lacking *Nos2* (Figure 7C). Based on these data, we conclude that during bacterial infection, adipocytes in PAT surrounding draining LNs can become infected and, in response to IFN-γ signaling, express iNOS and clear intracellular bacteria.

DISCUSSION

We have identified a central role for IFN-γ signaling and the subsequent production of NO by perinodal adipocytes in host-pathogen interactions. Our paper shows that *Lm* (and *Sa*), introduced via the skin, access draining LNs, presumably via the lymphatics, and infect the PAT. We speculate that this reflects transit of bacteria from the LNs to the PAT via the specialized conduits that have recently been described to provide a bidirectional route for fluids and cells to transit between these two tissues (Lin et al., 2018). We postulate that these conduits evolved to allow PAT innate immune cells to become engaged in an emerging immune response. AT has been reported to be a reservoir for HIV (Couturier and Lewis, 2018), *Trypanosoma cruzi* (Gonzalez et al., 2018), *Mycobacterium canettii* (Bouzid et al., 2017), and *Coxiella burnetii* (Bechah et al., 2014), and perhaps this supports the notion that pathogens that reach the responding LNs have access to the associated PAT. (It also indicates that these particular pathogens, unlike *Lm*, have evolved to evade protective mechanisms that exist within PAT.) An alternative mechanism of infection of PAT may be through the leakage of lymphatics en route to the LN, as was previously shown for mesenteric AT in mice infected with *Y. pseudotuberculosis* (Fonseca et al., 2015). Additional work would be required to determine which of these pathways to PAT infection is the case in our model, and to gain further insights about where within the AT the interactions described herein are occurring. Nevertheless, our studies highlight that sterilization of AT by adipocyte-intrinsic mechanisms induced by IFN-γ from immune cells following pathogen exposure is potentially key for restoring tissue homeostasis.

Our observation that loss of mature adipocytes or of FA mobilization from stored TAGs in adipocytes had no impact on the CD8$^+$ T cell response to *Lm* was unexpected. Previous reports had underscored the importance of AT deposits in the adaptive immune response, with visceral (Han et al., 2017) and bone marrow (Collins et al., 2019) AT acting as reservoirs for CD8$^+$ memory T cells following infection and dietary restriction, respectively. It is possible that in our studies the energy demands for acute lymphocyte activation and proliferation were met through systemic release of FAs from TAGs stored in the liver in the *Pparg*$^{fl/fl}$ *Adipoq*-Cre^{ERT2} mice, or from ATGL-independent mechanisms in the *Pnpla2*$^{fl/fl}$ *Adipoq*-Cre mice. Nevertheless, our data suggest that the CD8$^+$ T cell response associated with a localized, acute bacterial infection does not depend on AT-derived lipids. However, it remains possible that there is a role for PAT-derived FAs in the CD8$^+$ T cell response during chronic or secondary infections, and/or that a more detailed study would reveal roles in aspects of the CD4$^+$ T cell or B cell response.

Our data indicate that both *Lm* and *S. aureus* infection induce the expression of iNOS in PAT. *Mycobacterium tuberculosis*, upon infiltration of gonadal AT, has also been reported to induce iNOS expression in non-immune cells; however, the identity of those cells was not elucidated (Beigier-Bompadre et al., 2017).

(I) ^{13}C-glucose (yellow), ^{13}C-glutamine (orange), ^{13}C-palmitate (salmon), and ^{13}C-arginine (green) were independently traced using triple quad LC-MS. Fractional contribution of labeled carbons was calculated using peak area for the displayed metabolites.

(J) Nitrite levels in the supernatant quantified by Griess reaction in complete media (CM) or arginine-free (-arg) media.

(K) OCR was quantified using a Seahorse bioanalyzer and normalized to uninfected.

Statistical significance was calculated using two-tailed Student's t test (*$p < 0.05$, **$p < 0.005$, ***$p < 0.0005$, ****$p < 0.00005$, treatment versus uninfected; A, B, D–H, J, and K) or negative binomial regression (D2 or D3 vs D1; C). Mean ± SEM from three to six biological replicates. Data are representative of at least three individual experiments.

In addition, chronic TNF signaling has been reported to induce the expression of *Nos2* mRNA in adipocytes (Cheng et al., 2019); however, our data suggest that TNF, in contrast to IFN-γ, is insufficient to induce substantial iNOS expression. In addition, we observe that LPS is insufficient to induce iNOS expression in the presence of IFN-γ, while other groups testing LPS, IFN-γ, and TNF together found that this combination was able to upregulate iNOS expression in adipocytes *in vitro*, although the *in vivo* implications were not explored (Kapur et al., 1999).

We found that infection with *Lm in vivo* activated an immune-like gene expression network in adipocytes. Inflammatory gene signatures have been reported in adipocytes studied in the setting of obesity, which is widely considered a disease of chronic inflammation. Adipocytes isolated from patients with obesity displayed inflammatory activation, including enhanced MHCII expression and antigen presentation to $CD4^+$ T cells (Deng et al., 2013). Our RNA-seq results indicated that acute bacterial infection results in diminished expression of genes involved in core adipocyte functions, such as lipid metabolism, which could be due to increased levels of superoxide and impaired mitochondrial function (Jeon et al., 2012; Penfornis and Marette, 2005). This observation of inflammatory activation in non-immune cells adds to a growing list of studies identifying an active role for stromal cells in immune effector responses, and adds to the immunological repertoire of adipocytes and preadipocytes, which can become engaged in immune responses through the production of cytokines such as IL-6 and IL-33 (Brestoff and Artis, 2015; Caputa et al., 2019; Mahlakoiv et al., 2019). In this way, adipocytes and AT can be viewed as an additional immunoresponsive layer of protection to pathogen exposure.

We find that infiltration of PAT by bacteria activates NK and iNKT cells to supply the IFN-γ necessary for activation of an antimicrobial program in adipocytes. This is consistent with early work that stressed the importance of NK cells, activated by IL-12 and TNF to make IFN-γ, in providing initial control of *Lm* infection (Unanue, 1997). We speculate that the strong macrophage/monocyte and neutrophil responses to infection in PAT evident in the scRNA-seq data may reflect the involvement of these cells as producers of IL-12 and TNF to activate NK cells in this tissue. Our data raise the possibility that adipocytes could directly contribute to the activation of iNKT cells through the generation of the iNKT cell-activating lipid galactosylceramide (a hexosylceramide), and the associated expression of the MHC-like presentation machinery, *Cd1d*. Previous reports also demonstrated that adipocytes are capable of making glucosylceramides (Rakhshandehroo et al., 2019) and further showed that they can present lipid antigen to iNKT cells *in vitro* (Huh et al., 2013). Additional work will be required to determine whether the hexosylceramide that we detected is α or β-linked; this is important since the former are more stimulatory, and the ability of mammalian cells to make α-hexosylceramides has been questioned (Brennan et al., 2017). Interestingly, NKT cell antigens have been identified in *Lm* (Wolf et al., 2015). While NK cells are a known source of IFN-γ in AT upon infection (Teixeira et al., 2016), iNKT cells, while participating in the antimicrobial response in other tissues (Berzins et al., 2011), have mainly been studied in the context of AT metabolic homeostasis (Lynch et al., 2012), and it would be of interest to determine whether they play a role in restoring AT homeostasis following infection.

The combination of IFN-γ and infection with *Lm* promoted significant metabolic remodeling in adipocytes that is reminiscent of that described in macrophages and dendritic cells stimulated with IFN-γ plus TLR agonists (Jha et al., 2015; Everts et al., 2012). First, the production of NO leads to diminished respiration associated with a disrupted TCA cycle, and a compensatory increase in aerobic glycolysis to support ATP production (O'Neill and Pearce, 2016; Van den Bossche et al., 2017). Second, the TCA cycle, aspartate-arginosuccinate shunt, and urea cycle interact to support NO production. In adipocytes, this is clearly supported by L-arginine uptake. Interestingly, NO from macrophages has been shown to be sufficient to induce changes in adipocyte differentiation and to induce mitochondrial dysfunction (Jang et al., 2016; Yin et al., 2015). Thus, NO can clearly diffuse into adipocytes, which is consistent with its recognized ability to cross lipid bilayers. Nevertheless, adipocytes have evolved to be capable of making their own NO and thereby can independently control intracellular bacterial infection independently of macrophages. Moreover, our data indicate that the production of NO by adjacent immune cells is insufficient to clear *Lm* from infected adipocytes. We speculate that this may reflect specific requirements associated with the need to reach sterilizing concentrations of NO within a cell as large as an adipocyte. Further, we postulate that the fact that bacteria were cleared more quickly in adipocytes compared to in the SVF or PLN populations may be because adipocytes are a homogeneous population of cells within which all are capable of expressing iNOS, whereas there are numerous cell types in the heterogeneous SVF and PLN populations that cannot express iNOS and therefore require input from other cell types to resolve infection.

Our data show that in response to distal bacterial infection, adipocytes in PAT surrounding responding draining LNs can become infected and respond via intrinsic NOD-mediated mechanisms and extrinsic signals in the form of IFN-γ provided by immune cells, to express iNOS and make NO. This contributes to the control of infection and sterilization of the tissue. As part of this process, changes in gene expression and core metabolic processes in the adipocytes switch them away from their normal metabolic functions toward a more immunological role as the AT fights infection. The fate of infected adipocytes after they have controlled *Lm* is unknown. They could be replaced *in situ* by adipocytes newly differentiated from preadipocytes (Merrick et al., 2019), or they may persist. In the latter case, it is possible that, as in inflammatory macrophages (Van den Bossche et al., 2016), metabolic changes induced by the IFN-γ and *Lm*-induced anti-bacterial program are irreversible. This may impair future adipocyte and AT function once the infection is resolved and could therefore have a lasting impact on host systemic metabolism. Such metabolic tissue remodeling, due to excessive inflammation, might, for example, underlie short- and long-term metabolic alterations associated with COVID-19 syndrome (Ayres, 2020; Bruzzone et al., 2020; Wu et al., 2017). Our findings warrant examination of the long-term consequences of infection on AT biology.

Limitations of study

A limitation of this study is that it does not longitudinally follow the fate of adipocytes after infection has been cleared. Thus, at present we do not know whether gene expression is normalized and

the cells persist, or whether the cells that have engaged in immune responses die and are replaced by new adipocytes from the preadipocyte pool. The study leaves open the question of whether PAT is essential for *Listeria* clearance, or rather only provides assistance to the immune system. We did not explore the effects of a high-fat diet and associated weight gain on PAT biology, nor did we examine the biology of human PAT around responsive LNs. Whether PAT is involved in immune responses to other types of pathogens that do not infect PAT, or in allergic or autoimmune responses, remains to be explored.

STAR★METHODS

Detailed methods are provided in the online version of this paper and include the following:

- KEY RESOURCES TABLE
- RESOURCE AVAILABILITY
  - Lead contact
  - Materials Availability
  - Data and Code Availability
- EXPERIMENTAL MODEL AND SUBJECT DETAILS
  - Mouse models
  - Cell culture
- METHOD DETAILS
  - Tissue preparation
  - Generation of Nod1 Knockout 3T3L-1 cell line
  - Bacterial infection
  - RNA-seq, single cell RNA-seq and RT-qPCR
  - Western blot
  - Metabolic profiling
  - Nitric oxide production assay
  - *In vivo* depletion of NK and iNKT cells
  - Histology and microscopy
  - Flow cytometry
- QUANTIFICATION AND STATISTICAL ANALYSIS

SUPPLEMENTAL INFORMATION

Supplemental information can be found online at https://doi.org/10.1016/j.cmet.2022.04.008.

ACKNOWLEDGMENTS

We thank members of the Pearce laboratories, as well as Metabolomics, Deep Sequencing, and Imaging facilities at the Max Planck Institute of Immunobiology and Epigenetics, for technical support. This work was funded by the Max Planck Society, the German Research Foundation (DFG) SFB1160, DFG under Germany's Excellence Strategy (CIBSS EXC-2189 Project ID 390939984), Swiss National Science Foundation (to M.M. and M.A.S.), Japan Society for the Promotion of Science (to M.M.), Alexander von Humboldt Fellowship Foundation (to A.C., J.C., A.M.K., F.B., and M.V.), and Marie Skłodowska-Curie Actions (to J.C. and F.B.).

AUTHOR CONTRIBUTIONS

G.C., M.M., E.L.P., and E.J.P. conceptualized the study, designed the research, and interpreted the data. D.E.S. analyzed bioinformatics data. J.E.-H. analyzed metabolomics data. A.M.K. provided critical advice and performed experiments. P.H. helped with project insights. E.L.P. and E.J.P. acquired funding. K.M.G., R.P., M.A.S., A.C., J.C., A.J.F., P.A., M.S., N.v.T.B., M.V., F.B., A.Q., A.H., L.F., F.H., J.D.C., and A.E.P. performed specific experiments. G.C., M.M., and E.J.P. wrote the manuscript.

DECLARATION OF INTERESTS

E.J.P. and E.L.P. are founders of Rheos Medicines. E.L.P. is an SAB member of ImmunoMet.

Received: May 19, 2021
Revised: January 24, 2022
Accepted: April 13, 2022
Published: May 3, 2022

REFERENCES

Acedo, S.C., Gotardo, É.M.F., Lacerda, J.M., de Oliveira, C.C., de Oliveira Carvalho, P., and Gambero, A. (2011). Perinodal adipose tissue and mesenteric lymph node activation during reactivated TNBS-colitis in rats. Dig. Dis. Sci. *56*, 2545–2552. https://doi.org/10.1007/s10620-011-1644-8.

Aigouy, B., and Mirouse, V. (2013). ScientiFig: a tool to build publication-ready scientific figures. Nat. Methods *10*, 1048. https://doi.org/10.1038/nmeth.2692.

Ayres, J.S. (2020). A metabolic handbook for the COVID-19 pandemic. Nat. Metab. *2*, 572–585. https://doi.org/10.1038/s42255-020-0237-2.

Bechah, Y., Verneau, J., Ben Amara, A., Barry, A.O., Lepolard, C., Achard, V., Panicot-Dubois, L., Textoris, J., Capo, C., Ghigo, E., and Mege, J.L. (2014). Persistence of Coxiella burnetii, the agent of Q fever, in murine adipose tissue. PLoS One *9*, e97503. https://doi.org/10.1371/journal.pone.0097503.

Beigier-Bompadre, M., Montagna, G.N., Kuhl, A.A., Lozza, L., Weiner, J., 3rd, Kupz, A., Vogelzang, A., Mollenkopf, H.J., Lowe, D., Bandermann, S., et al. (2017). Mycobacterium tuberculosis infection modulates adipose tissue biology. Plos Pathog. *13*, e1006676. https://doi.org/10.1371/journal.ppat.1006676.

Berzins, S.P., Smyth, M.J., and Baxter, A.G. (2011). Presumed guilty: natural killer T cell defects and human disease. Nat. Rev. Immunol. *11*, 131–142. https://doi.org/10.1038/nri2904.

Bhardwaj, V., Heyne, S., Sikora, K., Rabbani, L., Rauer, M., Kilpert, F., Richter, A.S., Ryan, D.P., and Manke, T. (2019). snakePipes: facilitating flexible, scalable and integrative epigenomic analysis. Bioinformatics *35*, 4757–4759. https://doi.org/10.1093/bioinformatics/btz436.

Bouzid, F., Bregeon, F., Poncin, I., Weber, P., Drancourt, M., and Canaan, S. (2017). Mycobacterium canettii infection of adipose tissues. Front Cell Infect Microbiol *7*, 189. https://doi.org/10.3389/fcimb.2017.00189.

Brennan, P.J., Brigl, M., and Brenner, M.B. (2013). Invariant natural killer T cells: an innate activation scheme linked to diverse effector functions. Nat. Rev. Immunol. *13*, 101–117. https://doi.org/10.1038/nri3369.

Brennan, P.J., Cheng, T.Y., Pellicci, D.G., Watts, G.F.M., Veerapen, N., Young, D.C., Rossjohn, J., Besra, G.S., Godfrey, D.I., Brenner, M.B., and Moody, D.B. (2017). Structural determination of lipid antigens captured at the CD1d-T-cell receptor interface. Proc. Natl. Acad. Sci. U S A. *114*, 8348–8353. https://doi.org/10.1073/pnas.1705882114.

Brestoff, J.R., and Artis, D. (2015). Immune regulation of metabolic homeostasis in health and disease. Cell *161*, 146–160. https://doi.org/10.1016/j.cell.2015.02.022.

Bruzzone, C., Bizkarguenaga, M., Gil-Redondo, R., Diercks, T., Arana, E., Garcia de Vicuna, A., Seco, M., Bosch, A., Palazon, A., San Juan, I., et al. (2020). SARS-CoV-2 infection Dysregulates the metabolomic and lipidomic profiles of serum. iScience *23*, 101645. https://doi.org/10.1016/j.isci.2020.101645.

Buchmeier, N.A., and Schreiber, R.D. (1985). Requirement of endogenous interferon-gamma production for resolution of Listeria monocytogenes infection. Proc. Natl. Acad. Sci. U S A. *82*, 7404–7408. https://doi.org/10.1073/pnas.82.21.7404.

Caputa, G., Castoldi, A., and Pearce, E.J. (2019). Metabolic adaptations of tissue-resident immune cells. Nat. Immunol. *20*, 793–801. https://doi.org/10.1038/s41590-019-0407-0.

Chavez-Arroyo, A., and Portnoy, D.A. (2020). Why is Listeria monocytogenes such a potent inducer of CD8+ T-cells? Cell Microbiol. *22*, e13175. https://doi.org/10.1111/cmi.13175.

Cheng, A.W., Tan, X., Sun, J.Y., Gu, C.M., Liu, C., and Guo, X. (2019). Catechin attenuates TNF-alpha induced inflammatory response via AMPK-SIRT1 pathway in 3T3-L1 adipocytes. PLoS One *14*, e0217090. https://doi.org/10.1371/journal.pone.0217090.

Chouchani, E.T., and Kajimura, S. (2019). Metabolic adaptation and maladaptation in adipose tissue. Nat. Metab. *1*, 189–200. https://doi.org/10.1038/s42255-018-0021-8.

Clementi, E., Brown, G.C., Feelisch, M., and Moncada, S. (1998). Persistent inhibition of cell respiration by nitric oxide: crucial role of S-nitrosylation of mitochondrial complex I and protective action of glutathione. Proc. Natl. Acad. Sci. U S A. *95*, 7631–7636. https://doi.org/10.1073/pnas.95.13.7631.

Collins, N., Han, S.J., Enamorado, M., Link, V.M., Huang, B., Moseman, E.A., Kishton, R.J., Shannon, J.P., Dixit, D., Schwab, S.R., et al. (2019). The bone marrow protects and optimizes immunological memory during dietary restriction. Cell *178*, 1088–1101.e15. https://doi.org/10.1016/j.cell.2019.07.049.

Couturier, J., and Lewis, D.E. (2018). HIV persistence in adipose tissue reservoirs. Curr. HIV/AIDS Rep. *15*, 60–71. https://doi.org/10.1007/s11904-018-0378-z.

Deng, T., Lyon, C.J., Minze, L.J., Lin, J., Zou, J., Liu, J.Z., Ren, Y., Yin, Z., Hamilton, D.J., Reardon, P.R., et al. (2013). Class II major histocompatibility complex plays an essential role in obesity-induced adipose inflammation. Cell Metab *17*, 411–422. https://doi.org/10.1016/j.cmet.2013.02.009.

Dobin, A., Davis, C.A., Schlesinger, F., Drenkow, J., Zaleski, C., Jha, S., Batut, P., Chaisson, M., and Gingeras, T.R. (2013). STAR: ultrafast universal RNA-seq aligner. Bioinformatics *29*, 15–21. https://doi.org/10.1093/bioinformatics/bts635.

Everts, B., Amiel, E., van der Windt, G.J., Freitas, T.C., Chott, R., Yarasheski, K.E., Pearce, E.L., and Pearce, E.J. (2012). Commitment to glycolysis sustains survival of NO-producing inflammatory dendritic cells. Blood *120*, 1422–1431. https://doi.org/10.1182/blood-2012-03-419747.

Feingold, K.R., Doerrler, W., Dinarello, C.A., Fiers, W., and Grunfeld, C. (1992). Stimulation of lipolysis in cultured fat cells by tumor necrosis factor, interleukin-1, and the interferons is blocked by inhibition of prostaglandin synthesis. Endocrinology *130*, 10–16. https://doi.org/10.1210/endo.130.1.1370149.

Feingold, K.R., Soued, M., Staprans, I., Gavin, L.A., Donahue, M.E., Huang, B.J., Moser, A.H., Gulli, R., and Grunfeld, C. (1989). Effect of tumor necrosis factor (TNF) on lipid metabolism in the diabetic rat. Evidence that inhibition of adipose tissue lipoprotein lipase activity is not required for TNF-induced hyperlipidemia. J. Clin. Invest *83*, 1116–1121. https://doi.org/10.1172/JCI113991.

Fonseca, D.M., Hand, T.W., Han, S.J., Gerner, M.Y., Glatman Zaretsky, A., Byrd, A.L., Harrison, O.J., Ortiz, A.M., Quinones, M., Trinchieri, G., et al. (2015). Microbiota-dependent sequelae of acute infection compromise tissue-specific immunity. Cell *163*, 354–366. https://doi.org/10.1016/j.cell.2015.08.030.

Gonzalez, F.B., Villar, S.R., Toneatto, J., Pacini, M.F., Marquez, J., D'Attilio, L., Bottasso, O.A., Piwien-Pilipuk, G., and Perez, A.R. (2018). Immune response triggered by Trypanosoma cruzi infection strikes adipose tissue homeostasis altering lipid storage, enzyme profile and adipokine expression. Med. Microbiol. Immunol. *208*, 651–666. https://doi.org/10.1007/s00430-018-0572-z.

Han, S.J., Glatman Zaretsky, A., Andrade-Oliveira, V., Collins, N., Dzutsev, A., Shaik, J., Morais da Fonseca, D., Harrison, O.J., Tamoutounour, S., Byrd, A.L., et al. (2017). White adipose tissue is a reservoir for memory T cells and promotes protective memory responses to infection. Immunity *47*, 1154–1168.e6. https://doi.org/10.1016/j.immuni.2017.11.009.

Hotamisligil, G.S., Shargill, N.S., and Spiegelman, B.M. (1993). Adipose expression of tumor necrosis factor-α: direct role in obesity-linked insulin resistance. Science *259*, 87–91. https://doi.org/10.1126/science.7678183.

Huh, J.Y., Kim, J.I., Park, Y.J., Hwang, I.J., Lee, Y.S., Sohn, J.H., Lee, S.K., Alfadda, A.A., Kim, S.S., Choi, S.H., et al. (2013). A novel function of adipocytes in lipid antigen presentation to iNKT cells. Mol. Cell Biol. *33*, 328–339.

Jang, J.E., Ko, M.S., Yun, J.Y., Kim, M.O., Kim, J.H., Park, H.S., Kim, A.R., Kim, H.J., Kim, B.J., Ahn, Y.E., et al. (2016). Nitric oxide produced by macrophages inhibits adipocyte differentiation and promotes profibrogenic responses in preadipocytes to induce adipose tissue fibrosis. Diabetes *65*, 2516–2528. https://doi.org/10.2337/db15-1624.

Jeon, M.J., Leem, J., Ko, M.S., Jang, J.E., Park, H.S., Kim, H.S., Kim, M., Kim, E.H., Yoo, H.J., Lee, C.H., et al. (2012). Mitochondrial dysfunction and activation of iNOS are responsible for the palmitate-induced decrease in adiponectin synthesis in 3T3L1 adipocytes. Exp. Mol. Med. *44*, 562–570. https://doi.org/10.3858/emm.2012.44.9.064.

Jha, A.K., Huang, S.C., Sergushichev, A., Lampropoulou, V., Ivanova, Y., Loginicheva, E., Chmielewski, K., Stewart, K.M., Ashall, J., Everts, B., et al. (2015). Network integration of parallel metabolic and transcriptional data reveals metabolic modules that regulate macrophage polarization. Immunity *42*, 419–430. https://doi.org/10.1016/j.immuni.2015.02.005.

Kapur, S., Marcotte, B., and Marette, A. (1999). Mechanism of adipose tissue iNOS induction in endotoxemia. Am. J. Physiol. *276*, E635–E641. https://doi.org/10.1152/ajpendo.1999.276.4.E635.

Kohlgruber, A.C., LaMarche, N.M., and Lynch, L. (2016). Adipose tissue at the nexus of systemic and cellular immunometabolism. Semin. Immunol. *28*, 431–440. https://doi.org/10.1016/j.smim.2016.09.005.

Liao, Y., Smyth, G.K., and Shi, W. (2014). featureCounts: an efficient general purpose program for assigning sequence reads to genomic features. Bioinformatics *30*, 923–930. https://doi.org/10.1093/bioinformatics/btt656.

Lin, Y., Leung, G., Louie, D., Bogoslowski, A., Ross, J., Kubes, P., von der Weid, P.Y., and Liao, S. (2018). Perinodal adipose tissue participates in immune protection through a lymphatic vessel-independent route. J. Immunol. *201*, 296–305. https://doi.org/10.4049/jimmunol.1800151.

Love, M.I., Huber, W., and Anders, S. (2014). Moderated estimation of fold change and dispersion for RNA-seq data with DESeq2. Genome Biol. *15*, 550. https://doi.org/10.1186/s13059-014-0550-8.

Lynch, L., Nowak, M., Varghese, B., Clark, J., Hogan, A.E., Toxavidis, V., Balk, S.P., O'Shea, D., O'Farrelly, C., and Exley, M.A. (2012). Adipose tissue invariant NKT cells protect against diet-induced obesity and metabolic disorder through regulatory cytokine production. Immunity *37*, 574–587. https://doi.org/10.1016/j.immuni.2012.06.016.

MacMicking, J.D., Nathan, C., Hom, G., Chartrain, N., Fletcher, D.S., Trumbauer, M., Stevens, K., Xie, Q.W., Sokol, K., Hutchinson, N., et al. (1995). Altered responses to bacterial infection and endotoxic shock in mice lacking inducible nitric oxide synthase. Cell *81*, 641–650. https://doi.org/10.1016/0092-8674(95)90085-3.

MacQueen, H.A., and Pond, C.M. (1998). Immunofluorescent localisation of tumour necrosis factor-alpha receptors on the popliteal lymph node and the surrounding adipose tissue following a simulated immune challenge. J. Anat. *192* (Pt 2), 223–231. https://doi.org/10.1046/j.1469-7580.1998.19220223.x.

Macqueen, H.A., Waights, V., and Pond, C.M. (1999). Vascularisation in adipose depots surrounding immune-stimulated lymph nodes. J. Anat. *194* (Pt 1), 33–38. https://doi.org/10.1046/j.1469-7580.1999.19410033.x.

Mahlakoiv, T., Flamar, A.L., Johnston, L.K., Moriyama, S., Putzel, G.G., Bryce, P.J., and Artis, D. (2019). Stromal cells maintain immune cell homeostasis in adipose tissue via production of interleukin-33. Sci. Immunol. *4*, eaax0416. https://doi.org/10.1126/sciimmunol.aax0416.

Martin, M. (2011). Cutadapt removes adapter sequences from high-throughput sequencing reads. EMBnet J. *17*, 3. https://doi.org/10.14806/ej.17.1.200.

Mattacks, C.A., and Pond, C.M. (1997). The effects of feeding suet-enriched chow on site-specific differences in the composition of triacylglycerol fatty acids in adipose tissue and its interactions in vitro with lymphoid cells. Br. J. Nutr. *77*, 621–643. https://doi.org/10.1079/bjn19970061.

Matyash, V., Liebisch, G., Kurzchalia, T.V., Shevchenko, A., and Schwudke, D. (2008). Lipid extraction by methyl-tert-butyl ether for high-throughput lipidomics. J. Lipid Res. *49*, 1137–1146. https://doi.org/10.1194/jlr.D700041-JLR200.

McInnes, L., Healy, J., and Melville, J. (2018). UMAP: uniform manifold approximation and projection for dimension reduction. Preprint at arXiv. https://doi.org/10.48550/arXiv.1802.03426.

Merrick, D., Sakers, A., Irgebay, Z., Okada, C., Calvert, C., Morley, M.P., Percec, I., and Seale, P. (2019). Identification of a mesenchymal progenitor cell hierarchy in adipose tissue. Science *364*, eaav2501. https://doi.org/10.1126/science.aav2501.

Moro, K., Yamada, T., Tanabe, M., Takeuchi, T., Ikawa, T., Kawamoto, H., Furusawa, J.i., Ohtani, M., Fujii, H., and Koyasu, S. (2010). Innate production of T(H)2 cytokines by adipose tissue-associated c-Kit(+)Sca-1(+) lymphoid cells. Nature *463*, 540–544. https://doi.org/10.1038/nature08636.

Nieman, K.M., Kenny, H.A., Penicka, C.V., Ladanyi, A., Buell-Gutbrod, R., Zillhardt, M.R., Romero, I.L., Carey, M.S., Mills, G.B., Hotamisligil, G.S., et al. (2011). Adipocytes promote ovarian cancer metastasis and provide energy for rapid tumor growth. Nat. Med. *17*, 1498–1503. https://doi.org/10.1038/nm.2492.

O'Neill, L.A., and Pearce, E.J. (2016). Immunometabolism governs dendritic cell and macrophage function. J. Exp. Med. *213*, 15–23. https://doi.org/10.1084/jem.20151570.

O'Sullivan, D., van der Windt, G.J., Huang, S.C., Curtis, J.D., Chang, C.H., Buck, M.D., Qiu, J., Smith, A.M., Lam, W.Y., DiPlato, L.M., et al. (2014). Memory CD8(+) T cells use cell-intrinsic lipolysis to support the metabolic programming necessary for development. Immunity *41*, 75–88. https://doi.org/10.1016/j.immuni.2014.06.005.

Opitz, B., Puschel, A., Beermann, W., Hocke, A.C., Forster, S., Schmeck, B., van Laak, V., Chakraborty, T., Suttorp, N., and Hippenstiel, S. (2006). Listeria monocytogenes activated p38 MAPK and induced IL-8 secretion in a nucleotide-binding oligomerization domain 1-dependent manner in endothelial cells. J. Immunol. *176*, 484–490. https://doi.org/10.4049/jimmunol.176.1.484.

Pamer, E.G. (2004). Immune responses to Listeria monocytogenes. Nat. Rev. Immunol. *4*, 812–823. https://doi.org/10.1038/nri1461.

Patton, J.S., Shepard, H.M., Wilking, H., Lewis, G., Aggarwal, B.B., Eessalu, T.E., Gavin, L.A., and Grunfeld, C. (1986). Interferons and tumor necrosis factors have similar catabolic effects on 3T3 L1 cells. Proc. Natl. Acad. Sci. U S A. *83*, 8313–8317. https://doi.org/10.1073/pnas.83.21.8313.

Penfornis, P., and Marette, A. (2005). Inducible nitric oxide synthase modulates lipolysis in adipocytes. J. Lipid Res. *46*, 135–142. https://doi.org/10.1194/jlr.M400344-JLR200.

Pirzgalska, R.M., Seixas, E., Seidman, J.S., Link, V.M., Sanchez, N.M., Mahu, I., Mendes, R., Gres, V., Kubasova, N., Morris, I., et al. (2017). Sympathetic neuron-associated macrophages contribute to obesity by importing and metabolizing norepinephrine. Nat. Med. *23*, 1309–1318. https://doi.org/10.1038/nm.4422.

Pond, C.M. (1996). Interactions between adipose tissue and the immune system. Proc. Nutr. Soc. *55*, 111–126. https://doi.org/10.1079/pns19960014.

Rakhshandehroo, M., van Eijkeren, R.J., Gabriel, T.L., de Haar, C., Gijzel, S.M.W., Hamers, N., Ferraz, M.J., Boes, M., Kalkhoven, E., Aerts, J.M., et al. (2019). Adipocytes harbor a glucosylceramide biosynthesis pathway involved in iNKT cell activation. Biochim. Biophys. Acta Mol. Cell Biol. Lipids *1864*, 1157–1167. https://doi.org/10.1016/j.bbalip.2019.04.016.

Ramirez, F., Ryan, D.P., Gruning, B., Bhardwaj, V., Kilpert, F., Richter, A.S., Heyne, S., Dundar, F., and Manke, T. (2016). deepTools2: a next generation web server for deep-sequencing data analysis. Nucleic Acids Res. *44*, W160–W165. https://doi.org/10.1093/nar/gkw257.

Rath, M., Müller, I., Kropf, P., Closs, E.I., and Munder, M. (2014). Metabolism via arginase or nitric oxide synthase: two competing arginine pathways in macrophages. Front. Immunol. *5*, 532. https://doi.org/10.3389/fimmu.2014.00532.

Schneider, C.A., Rasband, W.S., and Eliceiri, K.W. (2012). NIH Image to ImageJ: 25 years of image analysis. Nat. Methods *9*, 671–675. https://doi.org/10.1038/nmeth.2089.

Schroder, K., Hertzog, P.J., Ravasi, T., and Hume, D.A. (2004). Interferon-γ: an overview of signals, mechanisms and functions. J. Leukoc. Biol. *75*, 163–189. https://doi.org/10.1189/jlb.0603252.

Silva, G.K., Gutierrez, F.R.S., Guedes, P.M.M., Horta, C.V., Cunha, L.D., Mineo, T.W.P., Santiago-Silva, J., Kobayashi, K.S., Flavell, R.A., Silva, J.S., and Zamboni, D.S. (2010). Cutting edge: nucleotide-binding oligomerization domain 1-dependent responses account for murine resistance against Trypanosoma cruzi infection. J. Immunol. *184*, 1148–1152. https://doi.org/10.4049/jimmunol.0902254.

Stuart, T., Butler, A., Hoffman, P., Hafemeister, C., Papalexi, E., Mauck, W.M., 3rd, Hao, Y., Stoeckius, M., Smibert, P., and Satija, R. (2019). Comprehensive integration of single-cell data. Cell *177*, 1888–1902.e21. https://doi.org/10.1016/j.cell.2019.05.031.

Teixeira, L., Marques, R.M., Ferreirinha, P., Bezerra, F., Melo, J., Moreira, J., Pinto, A., Correia, A., Ferreira, P.G., and Vilanova, M. (2016). Enrichment of IFN-gamma producing cells in different murine adipose tissue depots upon infection with an apicomplexan parasite. Sci. Rep. *6*, 23475. https://doi.org/10.1038/srep23475.

Unanue, E.R. (1997). Studies in listeriosis show the strong symbiosis between the innate cellular system and the T-cell response. Immunol. Rev. *158*, 11–25. https://doi.org/10.1111/j.1600-065x.1997.tb00988.x.

Van den Bossche, J., Baardman, J., Otto, N.A., van der Velden, S., Neele, A.E., van den Berg, S.M., Luque-Martin, R., Chen, H.J., Boshuizen, M.C., Ahmed, M., et al. (2016). Mitochondrial dysfunction prevents repolarization of inflammatory macrophages. Cell Rep. *17*, 684–696. https://doi.org/10.1016/j.celrep.2016.09.008.

Van den Bossche, J., O'Neill, L.A., and Menon, D. (2017). Macrophage immunometabolism: where are we (going)? Trends Immunol. *38*, 395–406. https://doi.org/10.1016/j.it.2017.03.001.

Vazquez-Boland, J.A., Kuhn, M., Berche, P., Chakraborty, T., Dominguez-Bernal, G., Goebel, W., Gonzalez-Zorn, B., Wehland, J., and Kreft, J. (2001). Listeria pathogenesis and molecular virulence determinants. Clin. Microbiol. Rev. *14*, 584–640. https://doi.org/10.1128/CMR.14.3.584-640.2001.

Weisz, A., Oguchi, S., Cicatiello, L., and Esumi, H. (1994). Dual mechanism for the control of inducible-type NO synthase gene expression in macrophages during activation by interferon-gamma and bacterial lipopolysaccharide. Transcriptional and post-transcriptional regulation. J. Biol. Chem. *269*, 8324–8333. https://doi.org/10.1016/s0021-9258(17)37197-1.

Williams, M.A., and Bevan, M.J. (2007). Effector and memory CTL differentiation. Annu. Rev. Immunol. *25*, 171–192. https://doi.org/10.1146/annurev.immunol.25.022106.141548.

Wolf, B.J., Tatituri, R.V.V., Almeida, C.F., Le Nours, J., Bhowruth, V., Johnson, D., Uldrich, A.P., Hsu, F.F., Brigl, M., Besra, G.S., et al. (2015). Identification of a potent microbial lipid antigen for diverse NKT cells. J. Immunol. *195*, 2540–2551. https://doi.org/10.4049/jimmunol.1501019.

Wolf, Y., Boura-Halfon, S., Cortese, N., Haimon, Z., Sar Shalom, H., Kuperman, Y., Kalchenko, V., Brandis, A., David, E., Segal-Hayoun, Y., et al. (2017). Brown-adipose-tissue macrophages control tissue innervation and homeostatic energy expenditure. Nat. Immunol. *18*, 665–674. https://doi.org/10.1038/ni.3746.

Wu, Q., Zhou, L., Sun, X., Yan, Z., Hu, C., Wu, J., Xu, L., Li, X., Liu, H., Yin, P., et al. (2017). Altered lipid metabolism in recovered SARS patients twelve years after infection. Sci. Rep. *7*, 9110. https://doi.org/10.1038/s41598-017-09536-z.

Yin, R., Fang, L., Li, Y., Xue, P., Li, Y., Guan, Y., Chang, Y., Chen, C., and Wang, N. (2015). Pro-inflammatory macrophages suppress PPARγ activity in adipocytes via S-nitrosylation. Free Radic. Biol. Med. *89*, 895–905. https://doi.org/10.1016/j.freeradbiomed.2015.10.406.

Zappia, L., and Oshlack, A. (2018). Clustering trees: a visualization for evaluating clusterings at multiple resolutions. Gigascience *7*, giy083. https://doi.org/10.1093/gigascience/giy083.

Zebisch, K., Voigt, V., Wabitsch, M., and Brandsch, M. (2012). Protocol for effective differentiation of 3T3-L1 cells to adipocytes. Anal Biochem. *425*, 88–90. https://doi.org/10.1016/j.ab.2012.03.005.

STAR★METHODS

KEY RESOURCES TABLE

REAGENT or RESOURCE	SOURCE	IDENTIFIER
Antibodies		
Monoclonal anti-mouse CD16/32 (clone: 93)	Biolegend	Cat#: 101302; RRID: AB_312801
Monoclonal anti-mouse CD3e-FITC (clone: 145-2C11)	Biolegend	Cat#: 100305; RRID: AB_312670
Monoclonal anti-mouse CD3e-BV785 (clone: 145-2C11)	Biolegend	Cat#: 100355; RRID: AB_2565969
Monoclonal anti-mouse CD4-FITC (clone: RM4-5)	Biolegend	Cat#: 100509; RRID: AB_312712
Monoclonal anti-mouse CD4-Alexa Fluor700 (clone: RM4-5)	Biolegend	Cat#: 100536; RRID: AB_493701
Monoclonal anti-mouse CD4-PE/Cyanine7 (clone: RM4-5)	Biolegend	Cat#: 100527; RRID: AB_312728
Monoclonal anti-mouse CD8a-PerCP/Cyanine5.5 (clone: 53–6.7)	Biolegend	Cat#: 100733; RRID: AB_2075239
Monoclonal anti-mouse CD8a-Alexa Fluor700 (clone: 53–6.7)	Biolegend	Cat#: 100730; RRID: AB_493703
Monoclonal anti-mouse CD45-PerCP/Cyanine5.5 (clone: 30-F11)	Biolegend	Cat#: 103132; RRID: AB_893340
Monoclonal anti-mouse CD19-APC/Cyanine7 (clone: 6D5)	Biolegend	Cat#: 115530; RRID: AB_830707
Monoclonal anti-mouse CD44-APC/Cyanine7 (clone: IM7)	Biolegend	Cat#: 103028; RRID: AB_830785
Monoclonal anti-mouse NK1.1-Pacific Blue (clone: PK136)	Biolegend	Cat#: 108722; RRID: AB_2132712
Monoclonal anti-mouse CD335-FITC (clone: 29A1.4)	Biolegend	Cat#: 137606; RRID: AB_2298210
Monoclonal anti-mouse CD1d-APC (clone: 1B1)	Biolegend	Cat#: 123521; RRID: AB_2715919
Monoclonal anti-mouse CD69-APC (clone: H1.2F3)	Biolegend	Cat#: 104514; RRID: AB_492843
Monoclonal anti-mouse CD62L-Pacific Blue (clone: MEL-14)	Biolegend	Cat#: 104424; RRID: AB_493380
T-Select mouse CD1d tetramer-PE	MBL	Cat#: TS-MCD-1
T-Select I-A^bOVA$_{323-339}$ tetramer-PE	MBL	Cat#: TS-M710-1
Monoclonal anti-mouse Ki-67-PE/Cyanine7 (clone: SolA15)	ebioscience	Cat#: 25-5698-80; RRID: AB_11217689
Monoclonal anti-mouse IFNγ-Alexa Fluor488 (clone: XMG1.2)	Biolegend	Cat#: 505813; RRID: AB_493312
Monoclonal anti-mouse TNF-alpha-Alexa Fluor647 (clone: MP6-XT22)	Biolegend	Cat#: 506314; RRID: AB_493330
Rabbit monoclonal anti-iNOS	CST	Cat#: 13120; RRID: AB_2687529
Rabbit polyclonal anti-NOD1	Novus Biologicals	Cat#: NB100-56878; RRID: AB_837807
Rabbit polyclonal anti-Stat1	CST	Cat#: 9172; RRID: AB_2198300
Rabbit monoclonal anti-pStat1 (Tyr701) (clone: 58D6)	CST	Cat#: 9167; RRID: AB_561284
Mouse monoclonal anti-alpha-tubulin	Sigma-Aldrich	Cat#: T5168; RRID: AB_477579
Goat anti-rabbit IgG (H + L) HRP-conjugated	Thermo Fisher Scientific	Cat#: 31460; RRID: AB_228341
Goat anti-mouse IgG (H + L) HRP-conjugated	Thermo Fisher Scientific	Cat#: 31430; RRID: AB_228307
Monoclonal purified anti-mouse NK1.1 (clone: PK136)	Biolegend	Cat#: 108712; RRID: AB_313399
Monoclonal purified anti-Asialo-GM1 (clone: Poly21460)	Biolegend	Cat#: 146002; RRID: AB_2562206
Monoclonal anti-CD1d functional grade (clone: 1B1)	ebioscience	Cat#: 16-0011-85; RRID: AB_468839
Rat IgG2b kappa isotype control functional grade (clone: 3B149/10H5)	ebioscience	Cat#: 16-4031-85; RRID: AB_470152
Bacterial and virus strains		
Listeria monocytogenes (10403s strain)	Pearce Lab	N/A
Listeria monocytogenes expressing ovalbumin	Pearce Lab	N/A
Staphylococcus aureus, Newman D2C strain	ATCC	Cat#: 25904
Chemicals, peptides, and recombinant proteins		
Alt-R S.p. Cas9 Nuclease V3	IDT	Cat#: 1081059
Alt-R Cas9 Electroporation Enhancer	IDT	Cat#: 1075916
Collagenase type I	Sigma-Aldrich	Cat#: 17018029

(*Continued on next page*)

Continued

REAGENT or RESOURCE	SOURCE	IDENTIFIER
Collagenase type II	Sigma-Aldrich	Cat#: 17101015
Recombinant murine IFN-γ	Peprotech	Cat#: 315-05
Recombinant murine TNF-α	Peprotech	Cat#: 315-01A
Lipopolysaccharide from *Escherichia coli* O 111:B4	Sigma-Aldrich	Cat#: L4391
C12-iE-DAP	InvivoGen	Cat#: tlrl-c12dap
Nodinitib-1 (ML130)	Sigma-Aldrich	Cat#: SML0379; CAS#: 799264-47-4
Dexamethasone	Sigma-Aldrich	Cat#: D1756; CAS#: 50-02-2
Rosiglitazone	Sigma-Aldrich	Cat#: R2408; CAS#: 122320-73-4
Porcine insulin	Sigma-Aldrich	Cat#: I5523; CAS#: 12584-58-6
3-isobutyl-1-methylxanine	Sigma-Aldrich	Cat#: I5879; CAS#: 28822-58-4
LIVE/DEAD Fixable Aqua dead cell stain kit	Life Technologies	Cat#: L34957
TRIzol reagent	Invitrogen	Cat#: 15596018
1400W	Sigma-Aldrich	Cat#: W4262; CAS#: 214358-33-5
Hematoxylin and Eosin stain kit	Vector Laboratories	Cat#: H-3502
Methyl tert-butyl-ether	Rotisolv	Cat#: T175.2; CAS#: 1634-04-4
U-13C6 D-Glucose	Cambridge Isotope	Cat#: CLM-1396-10
13C5 L-Glutamine	Cambridge Isotope	Cat#: CLM-1822-H-0.1
U-13C6 L-Arginine	Cambridge Isotope	Cat#: CLM-2265-H-0.5
U-13C16 Palmitic acid	Cambridge Isotope	Cat#: CLM-409-0.5
Critical commercial assays		
Adipose tissue progenitor isolation kit	Miltenyi Biotec	Cat#: 130-106-639
Griess Reagent kit	Thermo Fisher Scientific	Cat#: G7921
SuperScript III reverse transcriptase	Invitrogen	Cat#: 18080044
iTaq universal probes supermix	Biorad	Cat#: 1725134
P4 Primary cell 4D-nucleofector X kit S	Lonza	Cat#: V4XP-4032
TruSeq stranded mRNA kit	Illumina	Cat#: 20020594
Chromium Next GEM Chip G Single Cell Kit	10x Genomics	Cat#: 1000127
Chromium Next GEM Single Cell 3′ Library and Gel Bead Kit v. 3.1	10x Genomics	Cat#: 1000269
Deposited data		
scRNA-sequencing data	This paper	GEO: GSE171328
RNAseq	This paper	GEO: GSE172033
Experimental models: Cell lines		
3T3-L1 cell line	ATCC	Cat# CL-173; RRID: CVCL_0123
Experimental models: Organisms/strains		
C57BL/6J mice	Jackson Laboratories	Strain #: 000664; RRID: IMSR_JAX:000664
C57BL/6J-Ly5.1 mice	Jackson Laboratories	Strain #: 002014; RRID: IMSR_CRL:494
Adipoq-Cre^{ERT2} mice	Jackson Laboratories	Strain #: 025124; RRID: IMSR_JAX:025124
Adipoq-Cre mice	Jackson Laboratories	Strain #: 028020; RRID: IMSR_JAX:028020
Pparg$^{fl/fl}$ mice	Jackson Laboratories	Strain #: 004584; RRID: IMSR_JAX:004584
Ifngr1$^{fl/fl}$ mice	Jackson Laboratories	Strain #: 025394; RRID: IMSR_JAX:025394
Pnpla2$^{fl/fl}$ mice	Jackson Laboratories	Strain #: 024278; RRID: IMSR_JAX:024278
Nos2$^{-/-}$ mice	Jackson Laboratories	Strain #:002609; RRID: IMSR_JAX:002609
Oligonucleotides		
See Table S1 for gRNAs	IDT	N/A
See Table S2 for qRT-PCR primers	Applied Biosystems	N/A

(*Continued on next page*)

Continued

REAGENT or RESOURCE	SOURCE	IDENTIFIER
Software and algorithms		
Wave software version 2.4	Agilent Technologies	https://www.agilent.com/en/product/cell-analysis/real-time-cell-metabolic-analysis/xf-software/seahorse-wave-controller-software-2-4-2-740903
FlowJo version 10	TreeStar	RRID: SCR_008520
GraphPad Prism version 7.0	GraphPad	RRID: SCR_002798
Zen blue version 2.3 and 3.2	Zeiss	RRID: SCR_013672
ScientiFig plugin	(Aigouy and Mirouse, 2013)	https://biii.eu/scientifig
ImageJ version 2.1.0/1.53c	(Schneider et al., 2012)	RRID: SCR_003070
DESeq2 version 1.28.1	(Love et al., 2014)	RRID: SCR_015687
Morpheus	Board Institute	RRID: SCR_014975
DeepTools	(Ramirez et al., 2016)	RRID: SCR_016366
Cutadapt	(Martin, 2011)	RRID: SCR_011841
STAR	(Dobin et al., 2013)	RRID: SCR_004463
FeatureCounts	(Liao et al., 2014)	RRID: SCR_012919
R version 3.6.3	Lucent Technologies	RRID: SCR_001905
Cell Ranger version 2.2	10x Genomics	RRID: SCR_017344
Seurat v. 3	(Stuart et al., 2019)	RRID: SCR_007322
Uni-form Mani-fold Approximation and Projection	(McInnes et al., 2018)	RRID: SCR_018217
Clustree	(Zappia and Oshlack, 2018)	RRID: SCR_016293
Other		
DMEM, high glucose, pyruvate	Gibco	Cat#: 41966052
DMEM/F12, no glutamine	Gibco	Cat#: 21331020
DMEM, no glutamine	Gibco	Cat#: 21969035
DMEM, no glucose	Gibco	Cat#: 11966025
DMEM medium for SILAC	Gibco	Cat#: 88364
Fetal bovine serum	Gibco	Cat#: 10099141; Lot: 1966175

RESOURCE AVAILABILITY

Lead contact

Further information and requests for resources and reagents should be directed to and will be fulfilled by the lead contact, Edward J. Pearce (epearce7@jhmi.edu).

Materials Availability

This study did not generate new unique reagents.

Data and Code Availability

Next generation sequencing data are publicly available and can be accessed at Gene Ontology Omnibus under GEO: GSE172034. Accession numbers for accessing scRNAseq and RNA seq data individually are listed in the key resources table. Original western blot images, flow cytometry data, microscopy data, or any additional information required to reanalyze the data reported in this paper will be shared by the lead contact upon request.

EXPERIMENTAL MODEL AND SUBJECT DETAILS

Mouse models

All mice strains were purchased from The Jackson Laboratory. *Pparg*$^{fl/fl}$*Adipoq*-Cre^{ERT2} mice were generated by crossing *Pparg*$^{fl/fl}$ (RRID: IMSR_JAX:004584) and *Adipoq*-Cre^{ERT2} (RRID: IMSR_JAX:025124). *Pnpla2*$^{fl/fl}$*Adipoq*-Cre and *Ifngr1*$^{fl/fl}$*Adipoq*-Cre mice were generated by crossing *Adipoq*-Cre (RRID: IMSR_JAX:028020) and *Pnpla2*$^{fl/fl}$ (RRID: IMSR_JAX:024278) or *Ifngr1*$^{fl/fl}$ (RRID: IMSR_JAX:025394) respectively. Mice were maintained and bred in individually ventilated cages under specific-pathogen-free conditions at the Max Planck Institute of Immunobiology and Epigenetics mouse facility. Mice were kept on an inverted 14/10 h light/dark cycle, fed *ab libitum* chow diet (Ssniff). Littermate controls were used by default in all experiments. For generation of

bone-marrow chimeras, bone marrow cells were collected from femurs and tibias of congenically marked C57BL/6J-Ly5.1 (RRID: IMSR_CRL:494) mice. Red blood cells were lysed in ammonium-chloride-potassium lysing buffer (ACK; Gibco). Recipient C57BL/6J (RRID: IMSR_JAX: 000664) and *Nos2*$^{-/-}$ (RRID: IMSR_JAX:002609) mice were lethally irradiated (5 Gray and 4.5 Gray separated by 3 h) and reconstituted by i.v. injection of 10^7 bone marrow cells from donors into recipient mice 2 h after the last irradiation. Chimeric mice were allowed to reconstitute for 8–9 weeks before infection. Mice were kept on an inverted 14/10 h light/dark cycle, fed *ab libitum* chow diet (Ssniff). For tamoxifen-induced deletion of Cre activity, mice were given daily i.p. injection of 2 mg tamoxifen (Sigma-Aldrich) dissolved in corn oil for 5 days. All experiments were performed using 7-10-week sex-matched adult mice with the approval of local and institutional regulations. Total number of mice analyzed for each experiment is detailed in the figure legends and in the respective methods section.

Cell culture

3T3-L1 (murine embryonic fibroblast) were purchased from American Type Culture Collection (ATCC). Primary preadipocytes were isolated using Adipocyte Tissue Progenitor Isolation kit (Miltenyi Biotec) according to the manufacturer's protocol. 3T3-L1 cells or primary preadipocytes from SVF were cultured and differentiated as previously described (Zebisch et al., 2012). In brief, preadipocytes were expanded, maintained, and seeded in basal DMEM (high glucose) with 10% fetal bovine serum (FBS), 2 mM L-glutamine, 100 U/ml penicillin and streptomycin and 1 mM sodium pyruvate (all Gibco). Media was replaced on day 0 and 2 with DMEM/F12 (Gibco) with 10% FBS, 2 mM L-glutamine, 100 U/ml penicillin and streptomycin and 1 mM sodium pyruvate (complete DMEM/F12) containing 0.5 μM dexamethasone, 0.5 mM 3-isobutyl-1-methylxanine, 1.7 μM porcine insulin, and 1 μM rosiglitazone (all Sigma). On day 4 and 6, complete DMEM/F12 media was supplemented with 1.7 μM porcine insulin. At day 7 post differentiation, mature adipocytes were used for further assays. Cells were kept under 5% CO_2, atmospheric oxygen, at 37°C in a humidified incubator.

METHOD DETAILS

Tissue preparation

Dissected adipose tissue was minced and digested in DMEM, 25 mM HEPES (Gibco), 2 mg/mL collagenase type I and II (Life Technologies) for 45 min at 37°C followed by addition of 2 mM EDTA (Life Technologies) for 15 min at 37°C. Digested samples were filtered through 100 μm cell strainers (BD bioscience), and centrifuged for 10 min at 200g. Floating adipocyte fraction was carefully removed and washed with wash buffer (PBS containing 1% FBS [Gibco] and 2 mM EDTA). SVF pellet was incubated in 1 mL ACK lysing buffer (Gibco) for 5 min at room temperature, washed and re-suspended in wash buffer.

Generation of Nod1 Knockout 3T3L-1 cell line

Alt-R crRNA and tracrRNA (180 pmol; Integrated DNA Technologies) were annealed for 5 min at 98°C. The resulting ribonuclearprotein (RNP) complex was incubated with 60 pmol Alt-R S.p. Cas9 Nuclease V3 (Integrated DNA Technologies). RNPs were electroporated into 3T3L-1 cell line using Amaxa 4D-Nucleofector CM-137 program (Lonza) in P4 Primary cell buffer (Lonza) in the presence of 2 μM Alt-R Cas9 electroporation enhancer (Integrated DNA Technologies). The following predesigned Alt-R CRISPR-Cas9 gRNA (IDT) were used (Integrated DNA Technologies): AGGATGCTTACGTGGACCTC (Design ID: Mm.Cas9.NOD1.1.AA), AAATTGCTCACTGCTCGCAC (Design ID: Mm.Cas9.NOD1.1.AC), GTGGGAGTGACAACCCAATG (Design ID: Mm.Cas9.NOD1.1.AF) or Ms.Cas9.GCGAGGTAT TCGGCTCCGCG (non-targeting control). Single cell clones were selected and grown for further assays.

Bacterial infection

Wild type *L. monocytogenes* (*Lm*; 10403s strain) and Lm expressing ovalbumin (LmOVA) were cultured in brain heart infusion (BHI) broth (Sigma Aldrich) to log phase for 16 h at 37°C. *S. aureus* (Newman strain) was grown in LB media to exponential log phase at 37°C. Bacterial concentration was estimated from measurements at OD_{600}. Mice were anesthetized with isoflurane and infected with subcutaneous injection of 1 x 10^6 colony forming units (CFU) or with equivalent volumes of PBS into the hind footpad (*Lm*) or into the ear (*S. aureus*). Mice were subjected to Echo-MRI for total lean and fat measurements and sacrificed on indicated days post infection. The entire popliteal fat was anatomically excised. Weights of adipose tissue and lymph node were measured. Adipocytes, SVF isolated from adipose tissue, and lymph node were homogenized using FastPrep-24 homogenizer (MP Biomedicals). Bacterial load was determined by 10-fold serial dilutions on BHI agar (Sigma Aldrich) and incubated at 37°C overnight.

For *in vitro Lm* infection, 3T3-L1 cells or inguinal preadipocytes were differentiated into mature adipocytes for 7 days after which the media was switched to DMEM with 10% FBS, 2 mM glutamine without antibiotics. Cells were infected for 1 h with *Lm* at an MOI of 50 or with heat-inactivated (HI; 80°C for 30 min) *Lm* adjusted to 10^7 CFU/mL, followed by overnight stimulation of recombinant murine IFN-γ (50 ng/mL; Peprotech), recombinant murine TNFα (50 ng/mL; Peprotech) or LPS (20 ng/mL; Sigma) in media containing 10 μM gentamicin (Sigma Aldrich). For treatment with *Nod1* agonist, cells were stimulated with IFN-γ in the presence of C12-iE-DAP (InvivoGen) at concentrations of 1, 10, 20 μg/mL. For *Nod1* inhibitor treatment, cells were stimulated with *Lm*, IFN-γ, and ML130 (Nodinitib-1; Sigma) at concentrations of 10, 20, 50 μM.

RNA-seq, single cell RNA-seq and RT-qPCR

Total RNA was extracted with TRIzol reagent (Invitrogen) and quantified using Qubit 2.0 (Thermo Fisher Scientific) according to the manufacture's protocol.

RT-qPCR

Single-strand cDNA was synthesized from total RNA using SuperScript III Reverse Transcriptase (Thermo Fisher Scientific) following manufacturer's instructions. Quantitative RT-PCR was performed on QuantStudio three or 5 (Thermo Fisher Scientific) using iTaq Universal Probes Supermix (Bio-Rad Laboratories) and the following Taqman probe sets (Applied Biosystems): *Pparg* (Mm01208835_m1), *Adipoq* (Mm00456425_m1), Lipe (Mm00495359_m1), *Lpl* (Mm00434764_m1), *Pnpla2* (Mm00503040_m1), *Plin1* (Mm00558672_m1), *Fabp4* (Mm00445878_m1), *Cd36* (Mm00432403_m1), *Cd86* (Mm004444540_m1), *Cd74* (Mm00658576_m1), *H2-Aa* (Mm00439211_m1), *Nod1* (Mm00805062_m1), *Cd80* (Mm00711660_m1), *Cd1d1* (Mm00783541_s1), *Nos2* (Mm00440502_m1), *Adgre1* (Mm00802529_m1), *Ifngr1* (Mm00599890_m1), *Il6* (Mm00446190_m1), *Fcgr1* (Mm00438874_m1), and *Hprt* (Mm03024075_m1). *Hprt* was used as a housekeeping gene for normalization and results were analyzed by $2^{-\Delta\Delta CT}$ method.

RNA sequencing

Libraries were prepared using the TruSeq stranded mRNA kit (Illumina) and sequenced in a HISeq 3000 (Illumina) by the Deep-Sequencing Facility at the Max Planck Institute for Immunobiology and Epigenetics. Sequenced libraries were processed in an in-house developed RNA sequencing pipeline (Bhardwaj et al., 2019) that employs deepTools for quality control (Ramirez et al., 2016), cutadapt for trimming (Martin, 2011), STAR (Dobin et al., 2013) for mapping, and featureCounts (Liao et al., 2014) to quantify mapped reads. Raw counts of mapped reads were processed in R v. 3.6.3 (Lucent Technologies) with DESeq2 v.1.28.1 (Love et al., 2014) to determine differentially expressed genes. Normalized read counts were visualized as heatmaps using Morpheus (Broad Institute).

Single cell RNA sequencing

Single cell suspensions of freshly isolated SVF were processed using Chromium Single Cell 3′ Library, Gel Beads, Chip and Library Kit v. 3.1 (10X Genomics) following the manufacturer's protocol. Libraries were sequenced on HiSeq 3000. Samples were demultiplexed and aligned using Cell Ranger 2.2 (10X genomics) to genome build GRCm38 to obtain a raw read count matrix of barcodes corresponding to cells and features corresponding to detected genes. Read count matrices were processed, analyzed, and visualized in R v. 3.6.3 using Seurat v. 3 (Stuart et al., 2019) with default parameters in all functions, unless specified. Poor quality cells, with low total unique molecular identifier (UMI) counts and high percent mitochondrial gene expression, were excluded. Filtered samples were normalized with a log transformation and integrated with the canonical correlation analysis (cca) approach followed by mutual nearest neighbors, using 50 principal components. Integrated gene expression matrices were visualized with a Uni-form Mani-fold Approximation and Projection (UMAP) (McInnes et al., 2018) as a dimensionality reduction approach. Resolution for cell clustering was determined by evaluating hierarchical clustering trees at a range of resolutions (0–1.2) with Clustree (Zappia and Oshlack, 2018), selecting a value inducing minimal cluster instability. Datasets were subsetted to include only specific cells based on gene expression. Subsetted datasets were then split along conditions and processed anew as described above. Differentially expressed genes between clusters were identified as those expressed in at least 25% of cells with a greater than 0.25 natural log fold change and an adjusted p value of less than 0.01, using the FindMarkers function in Seurat v.3 with all other parameters set to default.

Western blot

Cells were washed with ice-cold PBS and lysed in 1x Cell Lysis Buffer (Cell Signaling Technology) supplemented with 1 mM PMSF (Sigma). Samples were subjected to three rounds of freeze-thaw cycles and centrifuged at 20,000 g for 10 min at 4°C. Protein was quantified and normalized using BCA protein assay kit (Thermo Fisher Scientific) according to the manufacturer's protocol. Cleared protein lysates were denatured with 4x NuPAGE LDS Sample Buffer (Thermo Fisher Scientific) for 10 min at 70°C. Samples were loaded on NuPAGE or Bolt 4–12% Bis-Tris protein gels (Life Technologies) and transferred to nitrocellulose membranes using iBolt2 Dry Blotting System (Thermo Fisher Scientific) according to the manufacturer's protocols. Membranes were blocked with 5% (w/v) milk (Sigma) in 0.1% Tween 20 containing TBS followed by incubation with primary antibodies, iNOS (Thermo Fisher Scientific), NOD1 (Novus Biologicals), STAT1 (Cell Signaling Technologies), p-STAT1 (Tyr701; Cell Signaling Technologies), and α-tubulin (Cell Signaling Technologies) in TBS with 5% (w/v) BSA (Sigma) and 0.1% Tween 20 overnight at 4°C. Secondary HRP-conjugated antibody (Pierce) was incubated with 5% milk in 0.1% Tween 20 containing TBS and visualized using Super-Signal West Pico or Femto Chemiluminescent Substrate (Pearce) on Hyperfilm Mp (Millipore) or ChemiDoc MP Imaging System (Bio-Rad Laboratories).

Metabolic profiling

Seahorse

Oxygen consumption rates (OCR) and extracellular acidification rates (ECAR) were measured on Seahorse XFe96 extracellular flux analyzer (Agilent Technologies). *In vitro*-derived mature adipocytes from 3T3-L1 or inguinal preadipocytes were seeded at a concentration of 2000 cells on a 96-well seahorse plate and differentiated *in vitro* for 7 days. Mature adipocytes were infected, then media was changed to unbuffered RPMI 1640 media containing 10 mM glucose, 2 mM L-glutamine, and 1 mM sodium pyruvate. Appropriate wells were injected with 100 μM 1400W (Sigma Aldrich) at the desired time points. Raw data were analyzed using Wave Desktop Software (Agilent Technologies) and exported to GraphPad Prism (GraphPad Software, version 7.0).

Metabolite tracing and quantification

Day 7 differentiated 3T3-L1 cells were washed and cultured in DMEM (without glucose or glutamine) supplemented with 25 mM ^{13}C-glucose, 2 mM ^{13}C-L-glutamine, or 20 mM ^{13}C-palmitate (Cambridge Isotope Laboratories) for 24 h. SILAC media containing 0.2 mM L-lysine and 1.1 mM ^{13}C-L-arginine was for 24 h. Labeled cells were rinsed twice with ice-cold 0.9% NaCl (Sigma Aldrich). Polar metabolites were extracted with ice-cold methanol:acetonitrile:water extraction buffer (50:30:20; Rotisolv), and dried using

EZ-2 Elite evaporator (Genevac). Liquid chromatography (1290 infinity II UHPLC; Agilent Technologies) coupled tandem mass spectrometry (6495B; Agilent Technologies) or Gas chromatography coupled tandem mass spectrometry (5977; Agilent Technologies) were used for analysis of metabolites at the Metabolomics Core Facility of Max Plank Institute for Immunobiology and Epigenetics.

Lipid quantification

For lipid analysis, biphasic methanol and methyl *tert*-butyl ether (MTBE; Rotisolv) extraction protocol was performed as previously described (Matyash et al., 2008). Lipids were extracted for 1 h at 4°C with constant agitation, separated by centrifugation, and the upper organic phase was collected and dried using EZ-2 Elite evaporator. Samples were re-suspended in isopropanol:acetonitrile:water (2:1:1; Rotisolv) buffer, and analyzed on 1290 infinity II UHPLC with Triple Quad QQQ-MS (6495; Aligent Technologies). Lipids were analyzed at the Metabolomics Core Facility of Max Plank Institute for Immunobiology and Epigenetics.

Nitric oxide production assay

Supernatants were subjected to Griess Reagent kit (Thermo Fisher Scientific) according to the manufacture's protocol. Total nitrite was measured by spectrophotometric determination of OD_{595} and calculated against a standard curve.

In vivo depletion of NK and iNKT cells

Mice were intravenously injected with a control mouse IgG2a antibody (Biolegend) or a combination of 40 μg α-NK1.1 (Biolegend; clone PK136), 40 μg of α-CD1d (Biolegend; clone 1B1), and 35 μL of α-Asialo-GM1 (Biolegend; clone Poly21460) one day prior to *Lm* infection.

Histology and microscopy

Fat tissues were aseptically harvested and fixed in 10% neutral buffered formalin for 24 h. Tissues were embedded in paraffin, sectioned into 8-micron sections, slides were deparaffinized and rehydrated prior to staining with hematoxylin and eosin Y (Vector Laboratories) according to the manufacturer's protocol. Histology images were acquired with an Axiocam 305 (Zeiss). Images were processed using Zen blue software (Zeiss, version 2.3 and 3.2), and compiled using ScientiFig plugin (Aigouy and Mirouse, 2013) in ImageJ (version 2.1.0/1.53c). Scalebar indicating 500 μm were added to each image.

Flow cytometry

Single cell suspensions were prepared and homogenized. Erythrocytes were lysed using ACK lysis buffer (Thermo Fisher Scientific). Cells were blocked with α-CD16/32 (Fc block), and stained with LIVE/DEAD fixable viability dye (Thermo Fisher Scientifics), fluorochrome-conjugated antibodies: CD45-PerCP-Cy5.5 (30-F11), CD8a-PerCP-Cy5.5 or -Alexa Fluor700 (53–6.7), CD3e-BV785, -FITC or -BV785 (145-2C11), NK1.1-PAcBlue (PK136), CD4-FITC, -Alexa Fluor700 or -PE-Cy7 (RM4-5), CD19-APC-Cy7 (6D5), CD335-FITC (29A1.4), CD1d-APC (1B1), CD69-APC (H1.2F3), CD44-APC-Cy7 (IM7), CD62L-Pacific Blue (MEL-14), CD1d-aGalCer tetramer-PE (MBL), and I-$A^b$$OVA_{323-339}$ MHC-peptide tetramer-PE (MBL). Cells were fixed and permeabilized with Cytofix/Cytoperm (BD Biosciences). Antibodies against Ki67-PE-Cy7 (SolA15), IFNγ-AF488 or -APC (XMG1.2), and TNFα-Alexa Fluor467 (MP6-XT22) were diluted in 1x Perm/Wash buffer (BD Biosciences). Data were acquired on LSRFortessa (BD Biosciences) and analyzed with FlowJo 10 (TreeStar) software.

QUANTIFICATION AND STATISTICAL ANALYSIS

GraphPad Prism 7 (GraphPad) software was used for representations and statistical analysis. Results are represented as mean ± SEM. Comparison of two groups were calculated by unpaired two-tailed Student's t tests or negative binomial regression.